THE INFLUENCE OF SURFACE ROUGHNESS AND ITS GEOMETRY ON

DYNAMIC BEHAVIOR OF WATER DROPLETS

Nima Sadeghpour

Thesis Prepared for the Degree of

MASTER OF SCIENCE

UNIVERSITY OF NORTH TEXAS

December 2014

APPROVED:

Jiangtao Cheng, Major Professor
Reza Mirshams, Committee Member
Sheldon Shi, Committee Member
Yong Tao, Chair of the Department of
    Mechanical and Energy
    Engineering
Mark Wardell, Dean of the Toulouse
    Graduate School

Sadeghpour, Nima. *The Influence of Surface Roughness and Its Geometry on Dynamic Behavior of Water Droplets*. Master of Science (Mechanical and Energy Engineering), December 2014, 62 pp., 2 tables, 28 figures, references, 36 titles.

In this study the author reports the effects of surface roughness on dynamic behavior of water droplets on different types of rough structures. First, the influence of roughness geometry on the Wenzel/ Cassie-Baxter transition of water droplets on one-tier (solid substrates with Si micropillars) surfaces is studied (Chapter 3). In order to address distinct wetting behaviors of the advancing and receding motions, the author investigates the Wenzel/ Cassie-Baxter transition of water droplets on one-tier surfaces over a wide range of contact line velocities and droplet volumes in both advancing and receding movements. The discussions are strengthened by experimental results. According to the author's analysis, the advancing contact zone tends to follow the Cassie-Baxter behavior for a wider range of geometric ratios than the receding contact zone. Physical phenomena such as advancing contact line rolling mechanism and the pinning of the receding contact line are introduced to justify distinct transition points of the advancing and receding movements respectively. Based on the analysis provided in Chapter 3, the author experimentally investigates the contact line fluctuations and contact line friction coefficients of water droplets on smooth, one-tier, and two-tier (with carbon nanotubes (CNTs) grown on Si micropillars) surfaces in Chapters 4 and 5. Both the advancing and receding contact line fluctuations/friction coefficients have been measured, analyzed and compared on smooth, one-tier, and two-tier surfaces over a wide range of contact line velocities and droplet volumes. A comprehensive analysis is provided to explain the experimental observations.

ACKNOWLEDGEMENTS

I would like to express my deepest appreciation to all those who provided me the possibility to complete this thesis. Foremost, I give a special gratitude to my advisor Dr. Jiangtao Cheng for his aspiring guidance, invaluably constructive criticism and friendly advice during my research under his supervision. Moreover, I am sincerely grateful to my family members for all their support and help.

TABLE OF CONTENTS

LIST OF TABLES

LIST OF FIGURES

CHAPTER 1

INTRODUCTION

Wettability is one of the most important features of a solid surface. Many studies have been conducted to relate the wettability of a surface to its physical properties such as surface roughness and surface energy. In particular, hydrophobic surfaces which exhibit high water repellency have been a subject of great interest. Due to the low surface energy of these surfaces, water droplets are repelled. Hydrophobic surfaces refer to the substrates on which the static contact angle of the liquid droplets is greater than 90°. Hydrophobicity can be largely found in nature; for example, a lotus leaf is well-known for hydrophobicity. Studies have revealed that the lotus leaf exhibits large contact angles due to the intrinsic multiscale hierarchical micro-and nano-structures on its surface [1-5]. Scanning Electron Microscope (SEM) images of the lotus leaf demonstrate the combination of micro-and nano-structures (two levels of roughness) on the lotus leaf surface. Water repellency of the lotus leaf is known as the lotus effect.

Figure 1.1. Lotus effect.

Moreover, the surface of the lotus leaf is covered by a hydrophobic wax which reduces the surface energy between the lotus leaf and the water droplets. Therefore, hydrophobicity of the lotus leaf can be ascribed to its surface roughness and hydrophobic coatings. It is noteworthy that hydrophobic surfaces can be fabricated

1

artificially by mimicking the lotus leaf structure. Inducing surface roughness on top of a flat substrate to generate water repellent properties (hydrophobicity) is called biomimetic. Coating with low surface energy materials is a widely used method to create hydrophobic properties. Low surface energy coatings as well as micro and nanopatterned structures can be applied to create a hydrophobic substrate. Indeed, introducing microscale (or nanoscale) roughness onto a flat hydrophobic surface can significantly enhance hydrophobicity, i.e., superhydrophobicity [6-9]. The term superhydrophobicity refers to a substrate on which the static contact angle is larger than 150°. These surfaces demonstrate unique features such as strong water repellence, self-cleaning characteristics, small adhesion, and friction reduction [10-13]. Due to the distinct features, superhydrophobic surfaces have significant potentials for practical applications. Recent studies have observed continuous dropwise condensation of water vapor on micro and nanopatterned rough structures can result in higher heat transfer coefficients [14, 15].

1.1 Contact Angle

Contact angle is the angle that a liquid droplet makes with a surface. It is also the best criterion for analyzing the wettability of a solid surface and can be defined for a static or a dynamic droplet. For a moving droplet, the contact angle at the front of the droplet (advancing contact line) is larger than the contact angle at the back of it (receding contact line). The difference between advancing and receding contact angles is called contact angle hysteresis and is a measure of resistance against droplet motion. A higher contact angle hysteresis leads to a more difficult droplet movement.
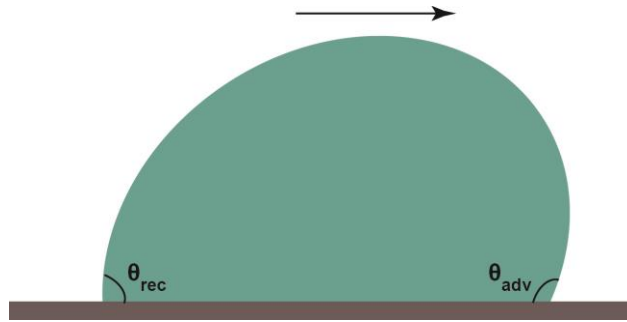
Figure 1.2. Advancing and receding contact angles.

Depending upon the contact angle of a droplet, solid substrates can be divided into three different categories: hydrophilic, hydrophobic, and superhydrophobic. If the contact angle is lower than 10°, the substrate is called hydrophilic. In this case, the droplet spreads out on the substrate, and the friction forces are considerable. If the contact angle is larger than 90°, the surface is considered as hydrophobic. The term superhydrophobic is reserved for substrates which exhibit contact angles greater than 150°.
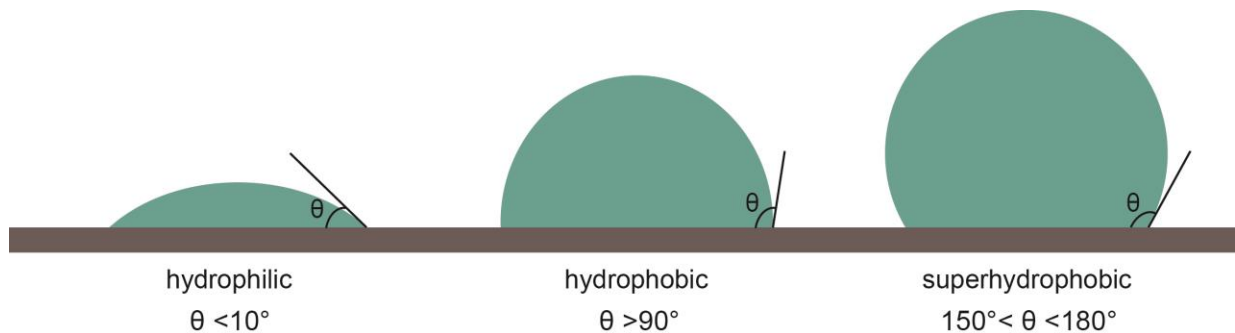
Figure 1.3. Different types of surfaces.

1.2 Young's Equation

Young's equation expresses the equilibrium contact angle on a solid surface as a function of surface energies between three different phases: gas-liquid, gas-solid, and solid-liquid. In other words, the contact angle for a static droplet in an ideal situation is

3

given by Young's equation. This equation can be derived by equating the total forces on the three-phase contact line to zero.
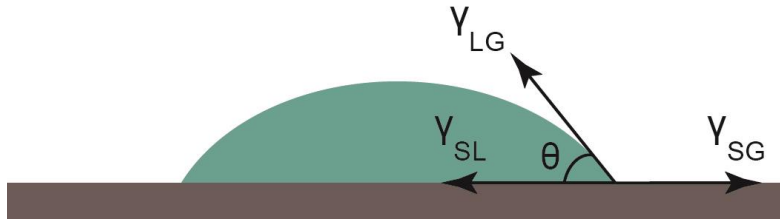
Figure 1.4. A droplet in equilibrium.

$$\sum F = \gamma_{SV} - \gamma_{SL} - \gamma_{LV} \cos \theta = 0 \tag{1.1}$$

Therefore, a relation for the contact angle of a droplet in equilibrium on a smooth surface can be ontained:

$$\cos \theta = \frac{\gamma_{SV} - \gamma_{SL}}{\gamma_{LV}} \tag{1.2}$$

The Young's equation can also be derived by exerting the equilibrium conditions for an infinitesimally small displacement of the contact line edge. For a stationary droplet, all three phases (liquid, vapor, and solid) are in equilibrium, and the global surface energy of the droplet is minimum. The contact angle of the droplet at equilibrium can be calculated by Young's equation. This relation can be also derived by analyzing the change in surface energy for an infinitesimally small displacement of the three-phase contact line (dx).
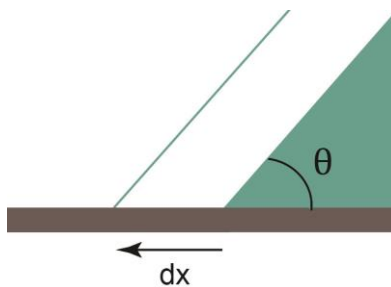
Figure 1.5. A contact line at equilibrium.

Assuming the contact angle of the droplet as θ, one can find the infinitesimal surface energy change of the three-phase contact line.

$$dE = dx \cos\theta\, \gamma_{LV} + dx\gamma_{SL} - dx\gamma_{SV} \tag{1.3}$$

It is notable that upon the infinitesimal displacement of the contact line, the liquid-vapor, solid-liquid, and solid-vapor interface areas change. At equilibrium, the total surface energy of the contact line should be minimum ($\frac{dE}{dx} = 0$). Therefore,

$$\cos\theta\, \gamma_{LV} + \gamma_{SL} - \gamma_{SV} = 0 \tag{1.4}$$

Therefore, Young's equation can be derived:

$$\cos\theta = \frac{\gamma_{SV} - \gamma_{SL}}{\gamma_{LV}} \tag{1.5}$$

It is important to note that this method is only applied on the equilibrium condition of the contact line leading edge, and it does not consider the entire water droplet (Fig. 1.5).

The wettability of a surface with roughness can be evaluated by two well-known models suggested by Wenzel [16] and Cassie-Baxter [17]. The fundamental concept of these two theories is based on the idea that the wetting behavior (contact angles) of a liquid droplet on a rough surface is a product of both the geometric characteristics of the rough surface and the wetting behavior (contact angle) of the same droplet on a smooth surface.

1.3 Wenzel Model

According to the Wenzel model, a droplet fills up the spaces between the asperities of a rough structure and as a result droplets following the Wenzel model are

largely pinned to the substrate. The Wenzel theory predicts the contact angle on a rough substrate as a function of the roughness geometry and the contact angle on the smooth substrate:

$$\cos\theta_w = r\cos\theta_0 \qquad (1.6)$$

where θ_w is the apparent contact angle of a Wenzel droplet on a rough surface, θ_0 is the Young's contact angle on a smooth surface, and r indicates the roughness factor of the solid surface.
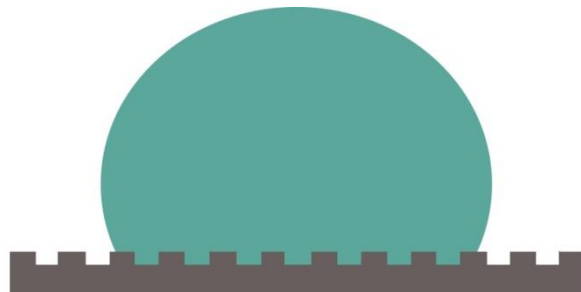

Figure 1.6. A Wenzel droplet.

Wenzel equation assumes that the water droplet fills up the cavities between the asperities of a rough surface. In this case, the Wenzel model predicts the contact angle which minimizes the surface energy change upon an infinitesimal displacement of the contact line.
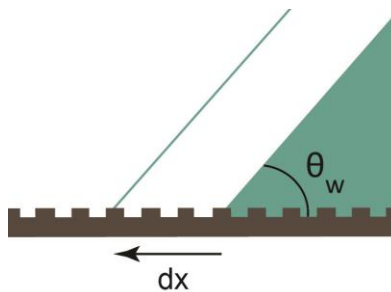

Figure 1.7. A droplet in Wenzel state.

$$dE = r\gamma_{SL}dx - r\gamma_{SV}dx + \gamma_{LV}dx\cos\theta_w \qquad (1.7)$$

The first term on the right hand side of the above equation corresponds to the increase in solid-liquid interface area upon infinitesimal movement of the contact line. The second term refers to the reduction in solid-vapor interface area and the third term indicates the change in liquid-vapor interface area. By equating the first derivative of dE to zero ($\frac{dE}{dx} = 0$), the contact angle that minimizes the total surface energy change of the contact line can be easily obtained:

$$r(\gamma_{SL} - \gamma_{SV}) + \gamma_{LV}\cos\theta_w = 0 \rightarrow \cos\theta_w = r\left(\frac{\gamma_{SV} - \gamma_{SL}}{\gamma_{LV}}\right) \qquad (1.8)$$

By combining the above relation with the Young's equation, the Wenzel relation is obtained.

$$\cos\theta_w = r\cos\theta_0 \qquad (1.9)$$

The above equation predicts the contact angle which a contact line at Wenzel state makes with the patterned substrate at equilibrium. Similar to the derivation of the Young's equation, this approach only exert the equilibrium condition on the contact line edge and do not consider the whole droplet. That is the reason the Wenzel equation is applicable for any state at equilibrium or local equilibrium. Let us consider a moving contact line. The droplet is locally in equilibrium on advancing and receding contact lines [18, 19]. Wenzel equation can be extended to predict the apparent advancing and receding contact angles due to the fact that the advancing and receding contact lines can be considered at local equilibrium. In the microscopic scale, the advancing contact angle is the angle at which the droplet is locally in equilibrium and the receding contact angle corresponds to the angle which keeps the receding motion at local equilibrium [18]. As the droplet advances on a substrate, the advancing contact angle minimizes the

local surface energy by exhibiting advancing contact angle. Similarly, the receding

contact line keeps the droplet at local equilibrium by showing receding contact angle (a

metastable state). On the receding case, the contact line needs to overcome the energy

barriers and move from one metastable state to the next one. But for an infinitesimal

displacement of the receding contact line, one can assume that the contact line is

locally in equilibrium. As mentioned before, in the process of derivation of the Wenzel

equation the focus was only on a contact line edge which is at equilibrium. Since the

advancing and receding contact lines are considered to be at local equilibrium [18, 19],

in both cases, the Wenzel equation for an infinitesimally small displacement of the

contact line edge can be rewritten. In the advancing case, the surface energy change is

$$dE_{adv} = r\gamma_{SL}dx_{adv} - r\gamma_{SV}dx_{adv} + \gamma_{LV}(\cos\theta_w)_{adv}dx_{adv} \tag{1.10}$$

Local criterion to obtain a minimum in surface energy change would be $\frac{dE_{adv}}{dx_{adv}} = 0$.

Therefore,

$$r(\gamma_{SL} - \gamma_{SV}) + \gamma_{LV}(\cos\theta_w)_{adv} = 0 \tag{1.11}$$

Hence,

$$(\cos\theta_w)_{adv} = r\left(\frac{\gamma_{SV} - \gamma_{SL}}{\gamma_{LV}}\right)_{adv} \tag{1.12}$$

Combining the above equation with the Young's relation, one can derive the Wenzel

equation for a locally stable advancing contact line as:

$$(\cos\theta_w)_{adv} = r(\cos\theta)_{0,adv} \tag{1.13}$$

Similarly, the infinitesimal surface energy change on the receding movement is $E_{rec} = r\gamma_{SL}dx_{rec} - r\gamma_{SV}dx_{rec} + \gamma_{LV}(\cos\theta_w)_{rec}dx_{rec}$. By minimizing the local surface energy for

the receding movement ($\frac{dE_{rec}}{dx_{rec}} = 0$), one can obtain

$$(\cos \theta_w)_{rec} = r \left(\frac{\gamma_{SV} - \gamma_{SL}}{\gamma_{LV}} \right)_{rec} \tag{1.14}$$

Therefore,

$$(\cos \theta_w)_{rec} = r(\cos \theta)_{0,rec} \tag{1.15}$$

Hence, one can apply the Wenzel equation for both advancing and receding movements.

The Wenzel relation was first proposed by Wenzel [16]. The roughness factor (r) is the ratio of the total surface area that is in contact with water over the total projected area:

$$r = \frac{\text{total surface area in contact with water}}{\text{total projected surface area}} \tag{1.16}$$

Therefore, for square pillars shown below one can obtain a formula for the roughness factor. The dashed red square is the repeated unit so the roughness factor of the repeated unit would be equal to the roughness factor of the whole structure. For the red dashed square the total surface area in contact with water would be equal to $4ah + (a + b)^2$. This includes the following areas:
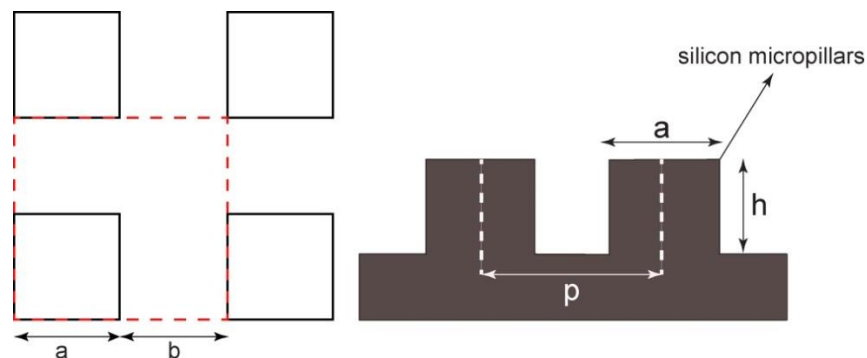
Figure 1.8. Schematic view of the one-tier surface.

- Four side walls of the pillar $(4ah)$
- Top of the pillar plus the space between the pillars $((a + b)^2)$

The total projected surface area would be equal to the area of the red dashed square $((a + b)^2)$. A formula for the roughness factor of the one-tier surface can be now derived:

$$r = \frac{4ah + (a + b)^2}{(a + b)^2} = \frac{4ah + p^2}{p^2} = 1 + \frac{4ah}{p^2} \qquad (1.17)$$

Hence, the Wenzel equation for a micropatterned rough structure decorated with square micropillars would be:

$$cos\theta_w = \left(1 + \frac{4ah}{p^2}\right)cos\theta_0 \qquad (1.18)$$

Since a Wenzel droplet is filling up the cavities between the pillars, the droplet movement would be sticky with a considerable contact angle hysteresis.

1.4 Cassie–Baxter Model

The Cassie–Baxter theory [17] assumes that the droplet stays on top of the asperities of a rough structure with air trapped between these asperities (Fig. 1.9). Owing to the existence of air pockets beneath a Cassie-Baxter droplet, the contact area of the droplet with the solid substrate would be significantly smaller than that of a Wenzel droplet. Therefore, droplet movement would be much easier in the Cassie-Baxter mode.
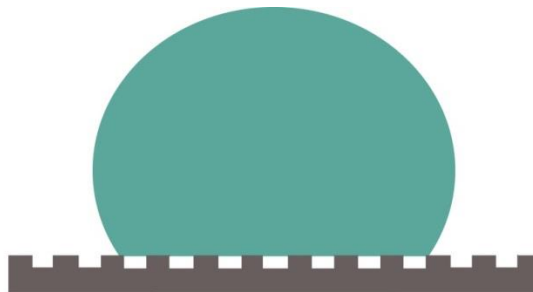
Figure 1.9. A Cassie-Baxter droplet.

10

The apparent contact angle of a Cassie droplet would be larger than the apparent contact angle of a Wenzel droplet. The Cassie-Baxter relation is

$$\cos \theta_{CB} = f \cos \theta_0 + (1 - f) \cos \theta_a \qquad (1.19)$$

where f is the solid fraction, θ_0 is the contact angle of the liquid droplet and the smooth substrate, and θ_a is the contact angle of water and air (This relation can be derived by minimizing the energy on the surface for an infinitesimal movement of the contact line). The contact angle between air and water is 180° ($\theta_a = 180°$). Therefore, the apparent contact angle of a droplet following the Cassie-Baxter model would be

$$\cos \theta_{CB} = f(\cos \theta_0 + 1) - 1 \qquad (1.20)$$

The Cassie-Baxter relation has been derived by minimizing the infinitesimal surface energy of a contact line which is standing on top of the asperities of a rough substrate.
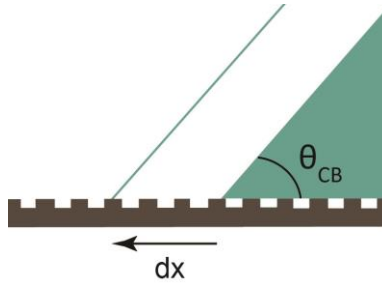
Figure 1.10. A droplet in Cassie-Baxter state.

$$dE = f\gamma_{SL}dx - f\gamma_{SV}dx + \gamma_{LV}dx \cos \theta_{CB} + (1 - f)\gamma_{LV}dx \qquad (1.21)$$

As a reminder, the solid-liquid fraction (f) is the ratio of the wetted solid surface to the total projected surface area. Upon an infinitesimal displacement of the contact line (dx), the solid-liquid interface area increases by $f\sigma_{sl}dx$. The solid-vapor interface area decreases by $f\gamma_{SV}dx$. It is notable that the term $(1 - f)\gamma_{LV}dx$ is associated with the

11

creation of air pockets beneath the water droplet. Now the equilibrium condition ($\frac{dE}{dx} = 0$)

is exerted on equation 1.21

$$f(\gamma_{SL} - \gamma_{SV}) + \gamma_{LV}\cos\theta_{CB} + (1-f)\gamma_{LV} = 0 \qquad (1.22)$$

Combining the above relation with the Young's equation

$$\cos\theta_{CB} = f(\cos\theta_0 + 1) - 1 \qquad (1.23)$$

The above equation is the Cassie- Baxter relation. For a moving droplet, since

the advancing and receding contact lines are considered to be at local equilibrium, one

can rewrite the Cassie-Baxter relation for both advancing and receding contact lines.

For an infinitesimal displacement of the advancing contact line edge, the change in

infinitesimal surface energy would be as

$$dE_{adv} = fdx_{adv}(\gamma_{SL} - \gamma_{SV}) + \gamma_{LV}(\cos\theta_{CB})_{adv}dx_{adv} + (1-f)\gamma_{LV}dx_{adv} \qquad (1.24)$$

Hence,

$$f\gamma_{SL} - f\gamma_{SV} + \gamma_{LV}(\cos\theta_{CB})_{adv} + (1-f)\gamma_{LV} = 0 \qquad (1.25)$$

And

$$(\cos\theta_{CB})_{adv} = f\left(\frac{\gamma_{SV} - \gamma_{SL}}{\gamma_{LV}}\right)_{adv} + (f-1) \qquad (1.26)$$

By applying the Young's equation

$$(\cos\theta_{CB})_{adv} = f[(\cos\theta)_{0,adv} + 1] - 1 \qquad (1.27)$$

Similarly the Cassie-Baxter relation for the receding contact line edge is derived as

below

$$(\cos\theta_{CB})_{rec} = f[(\cos\theta)_{0,rec} + 1] - 1 \qquad (1.28)$$

Now a mathematical relation for the solid fraction associated with square pillars should be derived. By definition, f is the ratio of total pillar-top surface area over total projected surface area:

$$f = \frac{\text{total pillar} - \text{top surface area in contact with water}}{\text{total projected surface area}} \tag{1.29}$$

The total pillar-top surface area is a^2. Thus, for the structure shown in Fig. 1.8, the solid fraction of the square pillars would be:

$$f = \frac{a^2}{(a+b)^2} = \frac{a^2}{p^2} \tag{1.30}$$

Hence, the Cassie-Baxter relation for a micropatterned rough structure decorated with square micropillars would be:

$$\cos\theta_{CB} = \frac{a^2}{p^2}(\cos\theta_0 + 1) - 1 \tag{1.31}$$

It is notable that Wenzel droplets demonstrate sticky features while the droplets following the Cassie-Baxter model exhibit slippery behaviors [20, 21].

1.5 Purpose of Study

Several studies have investigated the effects of roughness geometry on wettability of superhydrophobic surfaces and found that the geometric parameters of the micro and nanostructures such as width, height and spacing play a crucial role in the wetting properties of a textured surface [11-13]. It is reported that the advancing and receding contact lines can exhibit completely different dynamic behaviors on rough structures. Dorrer and Rühe [12] and Öner and McCarthy [13] have reported that the apparent advancing contact angles on a textured surface can be independent of the

geometry of the pillars. However, the receding contact angles are remarkably affected by the roughness geometry. Gao and McCarthy [22] stated that advancing and receding movements may have different activation energies. In this thesis, the author applied the Wenzel and Cassie–Baxter models to analyze the distinct dynamic behaviors of advancing and receding movements on micro- structured surfaces. The influence of roughness geometry on the transition of the Cassie mode to the Wenzel mode of water droplets on one-tier samples (with Si micropillars) for both advancing and receding zones was also investigated. Physical phenomena such as advancing contact line rolling mechanism and the pinning of the receding contact line are employed to explain different transition points of advancing and receding movements. The author also demonstrates that his theoretical discussion is in good agreement with his experimental results.

Moreover, the author has carried out an experimental analysis on contact line oscillations of water droplets on smooth, one-tier (with micropillars), and two-tier (with carbon nanotubes (CNTs) grown on micropillars) structures. The results have been plotted and compared all three types of substrates. The strong contact line pinning of the receding contact line on the one-tier surface leads to considerable fluctuations on the receding contact line/velocity. However, the oscillations on the smooth substrate are less than the one-tier surface due to the absence of surface roughness. Interestingly, the fluctuations on the two-tier surface are much less than the corresponding fluctuations on the smooth and one-tier surfaces. Finally, the influence of surface roughness on contact line friction coefficients of water droplets on micro- and nano-patterned surfaces has been reported. Both advancing and receding friction coefficients

have been measured, analyzed and compared on smooth, one-tier, and two-tier

surfaces over a wide range of contact line velocities and droplet volumes.

CHAPTER 2

EXPERIMENTAL PROCEDURE

In the provided experiments the researcher has utilized three types of surfaces: smooth, one-tier (with micropillars), and two-tier (with carbon nanotubes (CNTs) grown on micropillars) surfaces. Fig. 2.1 compares the schematic structure of these substrates.
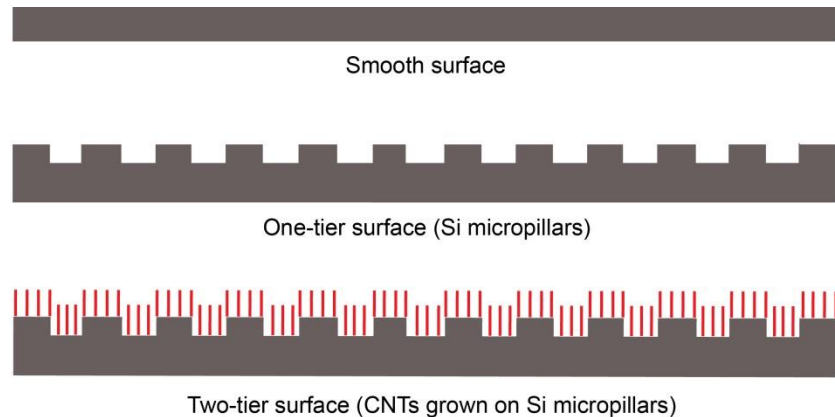
Figure 2.1. Smooth, one-tier, and two-tier structures.

The SEM images of the one-tier and two-tier structures are shown in Fig. 2.2. The one-tier surface only consists of micropillars but two-tier surfaces are artificially fabricated by integrating multiscale roughness on a flat substrate. First, square micropillars were formed on a smooth silicon substrate by deep reactive ion etching (DRIE), where a_m, h_m, and p_m are the width, height and pitch of the micropillars respectively (Fig. 2.2c). Then, a thin catalyst layer of nickel was deposited on the Si micropillars via e-beam evaporation. Carbon nanotubes (CNTs) were subsequently grown on top of the Si micropillars by plasma enhanced chemical vapor deposition (PECVD).

Figure 2.2. One-tier (a, b, and c) and two-tier (d, e, and f) structures. Images a, b, d, and e are captured by SEM ($a_m = 5\mu m$, $h_m = 4.75\mu m$, and $p_m = 9\mu m$). A thin layer of fluoropolymer is coated on the samples to generate hydrophobic features.

Coating with low-surface-energy materials is a widely used technique to generate hydrophobic properties on a solid substrate [23-25]. Hence, in order to create hydrophobic 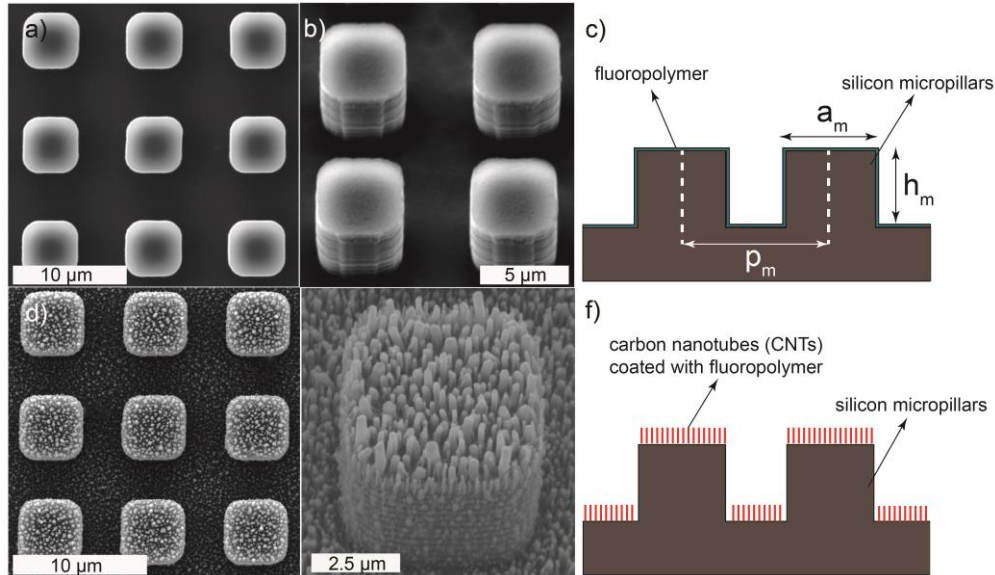or superhydrophobic surfaces, a thin layer of fluoropolymer PFC1601V (Cytonix) was uniformly coated on all samples leading to the apparent contact angles larger than $90°$ (hydrophobic) or $150⁰$ (superhydrophobic). Fig. 2.3 shows the schematic of the experimental set up. Initially, a micropipette was used to place a water microdroplet on a smooth hydrophobic substrate which was attached to a motorized translation stage (MTS50/M-Z8, Thorlabs). This smooth substrate was coated with a thin layer of fluoropolymer (PFC1601V, Cytonix) everywhere on its surface except for a tiny area of 1mm x 1mm under the center of the droplet. The hydrophilic properties of this small area beneath the droplet made the droplet stick to the substrate and move along with the translation stage. It is important to note that the entire shape of the droplet was not affected by this tiny hydrophilic area underneath and the droplet on the

substrate still exhibited a contact angle of ~123°, i.e., static contact angle on a smooth hydrophobic substrate. The velocity of the translation stage can be accurately controlled by its control system. The experiments were carried out with the following stage velocities: 0.25, 0.5, 0.75, 1.0, 1.5, 2.0, 2.5 and 3.0 mm/s. The smooth, one-tier, or two-tier samples were attached to a micrometer z-stage (NT66-495, Edmund Optics) above the droplet. Then the sample was gradually lowered until it slightly touched the droplet. A light beam (Dolan-Jenner MI-150 fiber optic illuminator) was adjusted at the back of the droplet (in front of the camera) for enhanced illumination. In this experimental setup, the top surface of the droplet slid on the sample coated with fluoropolymer while its bottom was adhered to the moving stage.
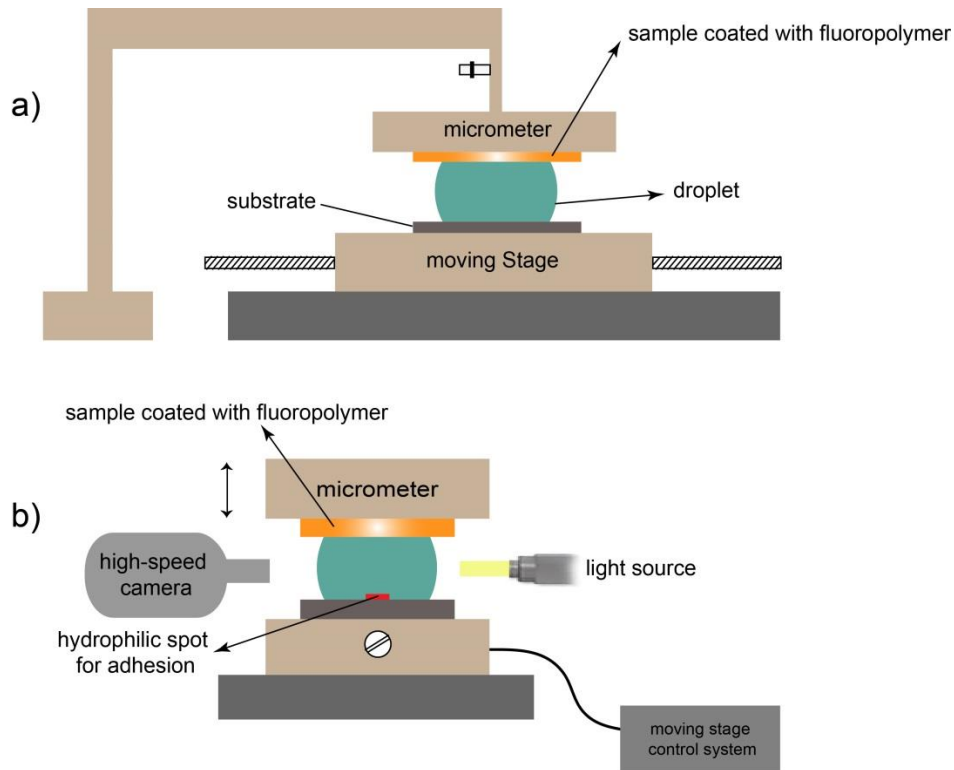
Figure 2.3. Schematic view of the experimental set up: a) front view, b) side view.

As can be seen in Fig. 2.4, the droplet was initially symmetric. During movement, due to the contact angle hysteresis the shape of the droplet became asymmetric and the advancing contact angle became larger than the receding contact angle. It is noteworthy that the effect of gravity was neglected since the droplet size was smaller than or on the order of its capillary length $\lambda_c = \sqrt{\dfrac{\gamma}{\rho g}} = 2.7$ mm, where γ is the surface tension of water with air, ρ is the water density, and g is the acceleration of gravity.
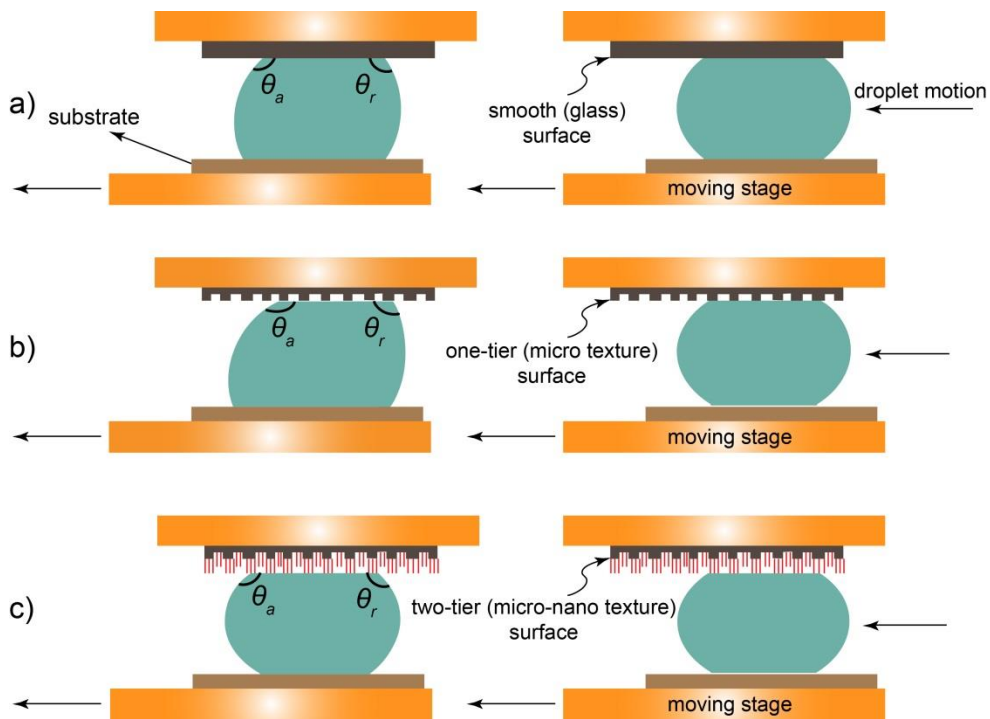
Figure 2.4. Movement of a droplet on smooth, one-tier, and two-tier surfaces.

In order to better investigate the dynamic behaviors of the advancing and receding contact lines on smooth, one-tier, and two-tier structures, the researcher has conducted his experiments with various volumes and transport velocities of water droplets. A high speed CCD camera (Phantom Miro M310) with frame rates up to 3200 frames/s was utilized to record the dynamic movements of both the advancing and the

receding edges on the water droplet. Image J, a Java image processing software, with

DropSnake plugin [26] was used to precisely measure the contact angles of the

recorded frames.

CHAPTER 3

TRANSITION BETWEEN WENZEL AND CASSIE-BAXTER REGIMES

3.1 Advancing and Receding Contact Angles

Fig. 3.1a, 3.1b, and 3.1c plot apparent contact angles versus contact line velocities on one-tier structures for water droplets of 15 μl, 25 μl , and 50 μl, respectively. The black data points represent the apparent advancing contact angles versus the advancing contact line velocities and the red data points denote the apparent receding contact angles versus receding contact line velocities. The advancing contact angles differed only slightly from the static contact angle (2° to 6.5°) while the receding contact angles changed by as much as 26° to 41°. To explain the distinct dynamic behaviors of the advancing and receding contact lines on one-tier samples, a comprehensive analysis is carried out in the discussion section. It is important to note that during the droplet movement the contact line edge fluctuates. Hence, oscillations of both the contact angle and the contact line velocity should be taken into account (The contact line oscillations will be discussed completely in chapter 4). It is noteworthy that the values shown in Fig. 3.1 are the averaged values of advancing and receding contact angles/velocities over time.

3.2 Dynamic Contact Angle Hysteresis

Dynamic contact angle hysteresis (CAH) is an important factor in determining the wetting properties of a solid surface and is defined as the difference between the dynamic advancing and dynamic receding contact angles at a specific velocity of a droplet [27, 28]. A smaller dynamic CAH leads to an easier contact line motion. Fig.

3.1d plots dynamic CAH versus the droplet velocity on one tier surfaces for water droplet of 15 μl, 25 μl , and 50 μl (Droplet velocity is estimated as the corresponding stage velocity). The provided measurements indicate that one-tier surfaces exhibit high dynamic CAH in the range of 28° to 45°. As mentioned before, the considerably large CAH on one-tier samples is due to the sticky behavior of the receding contact zone.
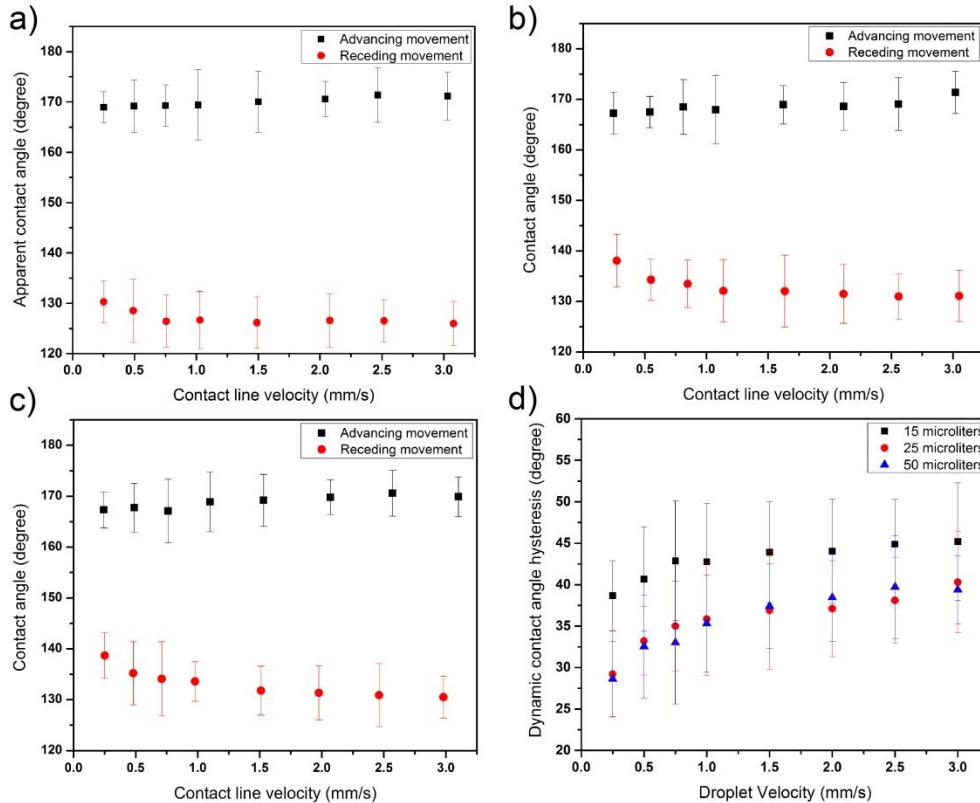
Figure 3.1. Apparent contact angle versus contact line velocity for advancing and receding movements of a water droplet of a) 15 μl, b) 25 μl, c) 50 μl. d) Dynamic CAH versus droplet velocity for water droplet of 15 μl, 25 μl , and 50 μl.

According to the experimental observations, the receding contact zone on one-tier surfaces exhibit sticky properties as evidenced by contact line oscillations. Fig. 3.2 illustrates the evolution of advancing and receding contact angles while the droplet slides on the one-tier substrate. The velocity of the moving stage was fixed at 3 mm/s and the 15 μl droplet is moving leftward. As can be seen in Fig. 3.2, there was only a

slight variation of ~ 4.6° in the advancing contact angle during the droplet motion on one-tier surfaces. In contrast, a significant change of 41.8° was observed in the receding contact angle that resulted in a considerably high dynamic CAH of 46.9°.

Figure 3.2. The evolution of the advancing and receding contact angles on one-tier surfaces (top substrate). The 15μl droplet is moving leftward and the velocity of the bottom stage is 3 mm/s.

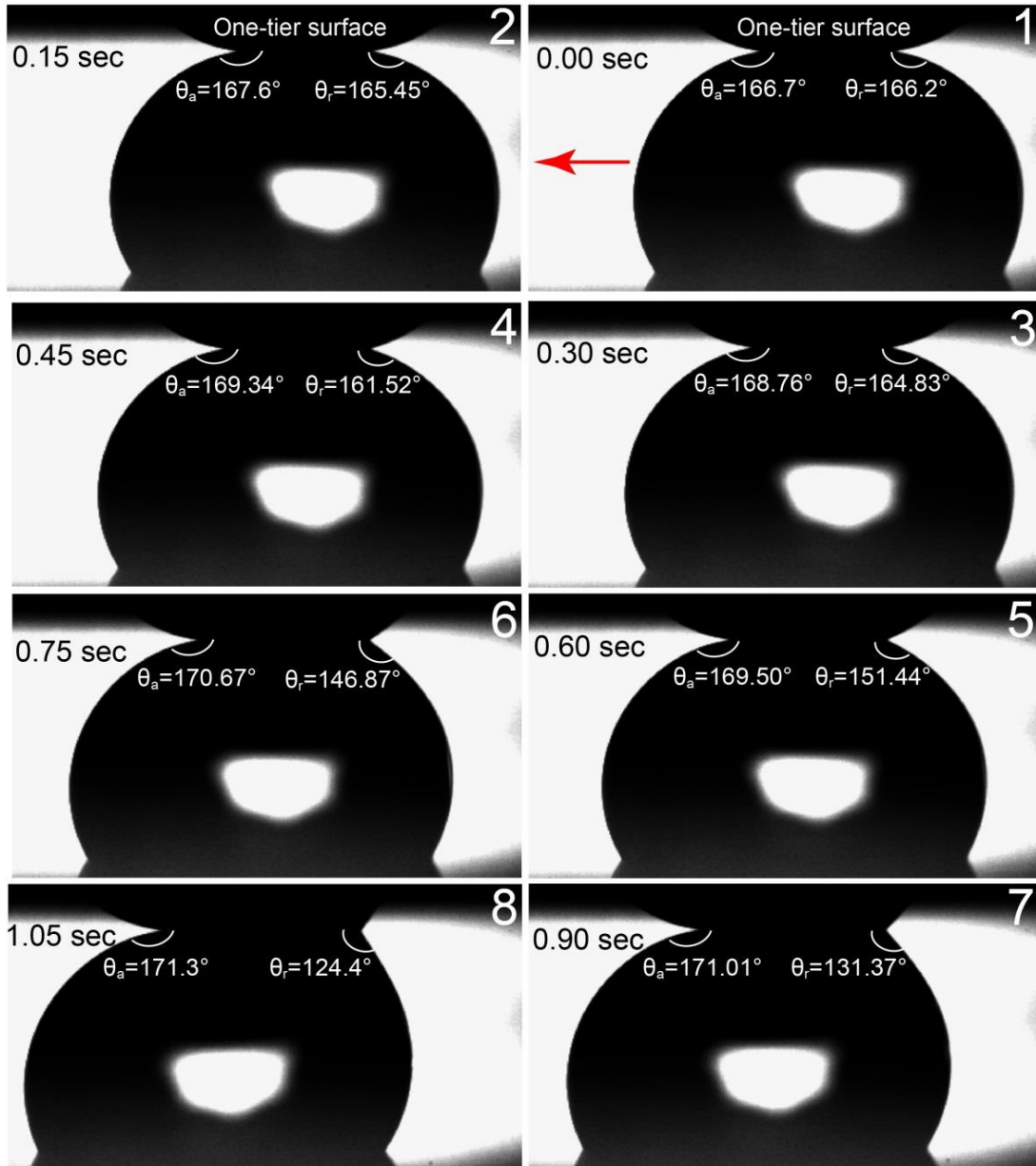In the following discussion, the remarkable contact angle hysteresis on one-tier surfaces is justified.

3.3 Discussion

Wettability of a textured structure can be analyzed by the Wenzel and the Cassie–Baxter models. As demonstrated in Chapter 1, for the one-tier micro-structures shown in Fig. 2.2, the following relations can be applied to calculate r_m and f_m :

$$r_m = 1 + \frac{4a_m h_m}{p_m^2} \tag{3.1}$$

$$f_m = \frac{a_m^2}{p_m^2} \tag{3.2}$$

where a_m, h_m, and p_m are the width, height and pitch of the square micropillars, respectively. Consequently, Wenzel and Cassie-Baxter equations can be rewritten as:

$$\cos\theta_w = (1 + \frac{4a_m h_m}{p_m^2})\cos\theta_0 \tag{3.3}$$

$$\cos\theta_{CB} = \frac{a_m^2}{p_m^2}(\cos\theta_0 + 1) - 1 \tag{3.4}$$

where θ_0 is the water contact angle on a smooth surface. The geometry of the micropillars plays an important role in the wetting behavior of a droplet and there exists a critical transition point which demarcates the Wenzel regime and Cassie–Baxter regime. In order to study the transition between these two modes, a parameter called spacing factor s_f is defined as below [29]:

$$s_f = \frac{a_m}{p_m} \tag{3.5}$$

In this work, micropillars have a specific ratio of $\frac{h_m}{a_m} = 0.95$ ($a_m = 5\mu m$ and $h_m = 4.75\mu m$). Therefore, Wenzel and Cassie–Baxter equations can be rewritten as functions of the spacing factor s_f^2:

$$\cos\theta_w = \left(1 + 3.8s_f^2\right)\cos\theta_0 \tag{3.6}$$

$$\cos\theta_{CB} = s_f^2(\cos\theta_0 + 1) - 1 \tag{3.7}$$

The above equations can be extended to differentiate the advancing and receding movements of a droplet on a rough surface. We use $\theta_{0,adv}$ and $\theta_{0,rec}$ to stand for the advancing and the receding contact angles on the smooth hydrophobic surface, respectively. According to the measurements, $\theta_{0,adv}/\theta_{0,rec}$= 135°/110°. Thus, the advancing and receding contact zones can have distinct Wenzel-Cassie transition points. In order to better investigate the transitions between the Wenzel and Cassie–Baxter regimes, $\cos\theta$ versus s_f^2 is plotted for both the advancing and receding cases. (equations 3.6 and 3.7).

Fig. 3.3a illustrates the transition between the Cassie and Wenzel states in the receding transport of a water droplet on one-tier surfaces ($\theta_{0,rec} = 110°$). The receding Wenzel-Cassie transition occurs at $s_f^2 = 0.34$ (the one-tier samples have $s_f^2 = 0.3$). The solid lines in Fig. 3.3a represent the stable Wenzel and stable Cassie states. Therefore, the droplets have a lower free energy along the solid lines. The dashed line represents the metastable Cassie state and the total energy of the metastable Cassie mode is considerably higher than the stable Wenzel mode. The vertical arrows indicate the transformation of a droplet in the metastable Cassie regime to the stable Wenzel regime in order to achieve a lower free energy [29]. The black circles in Fig. 3.3a represent the

experimental measurements in the receding case. The position of the circles is determined by the spacing factor (s_f) and the measured receding contact angles on one-tier substrates. Owing to the propinquity of the Wenzel state line and the black circles, the receding movement on one-tier surfaces is considered in the Wenzel state (since $s_f^2 < 0.34$). Wenzel droplets are known by a large contact angle hysteresis and sticky behaviors. Indeed, the provided experiments demonstrate that the receding contact zone behavior on one-tier substrates was highly sticky and a relatively large contact angle hysteresis in the range of 28°-45° was observed. It is noteworthy that after placing the water droplet on one-tier surfaces, the receding contact zone may be initially in the metastable Cassie state. As the droplet starts to move in response to an external shear force, the receding zone departs from the metastable Cassie regime and transits to the stable Wenzel state in order to maintain a lower free energy as shown by the vertical arrows in Fig. 3.3a. Fig. 3.3b illustrates the transition between Wenzel and Cassie regimes in the advancing contact zone with $\theta_{0,adv} = 135°$. The advancing Cassie-Wenzel transition occurs at $s_f^2 = 0.098$. The black circles in Fig. 3.3b indicate the experimental values in the advancing case on one-tier surfaces. The position of these circles is determined by both the spacing factor s_f and the experimentally measured advancing contact angles on one-tier samples. Owing to the closeness of the Cassie line and the experimental values, the advancing movement on one-tier substrates can be considered in the Cassie–Baxter mode. Unlike the receding case, the advancing contact line/zone stays at the lower free energy state (stable Cassie regime) during the droplet motion. Only a slight difference between the static and dynamic contact angles was observed on the advancing contact zone (~ 2° to 6.5°).
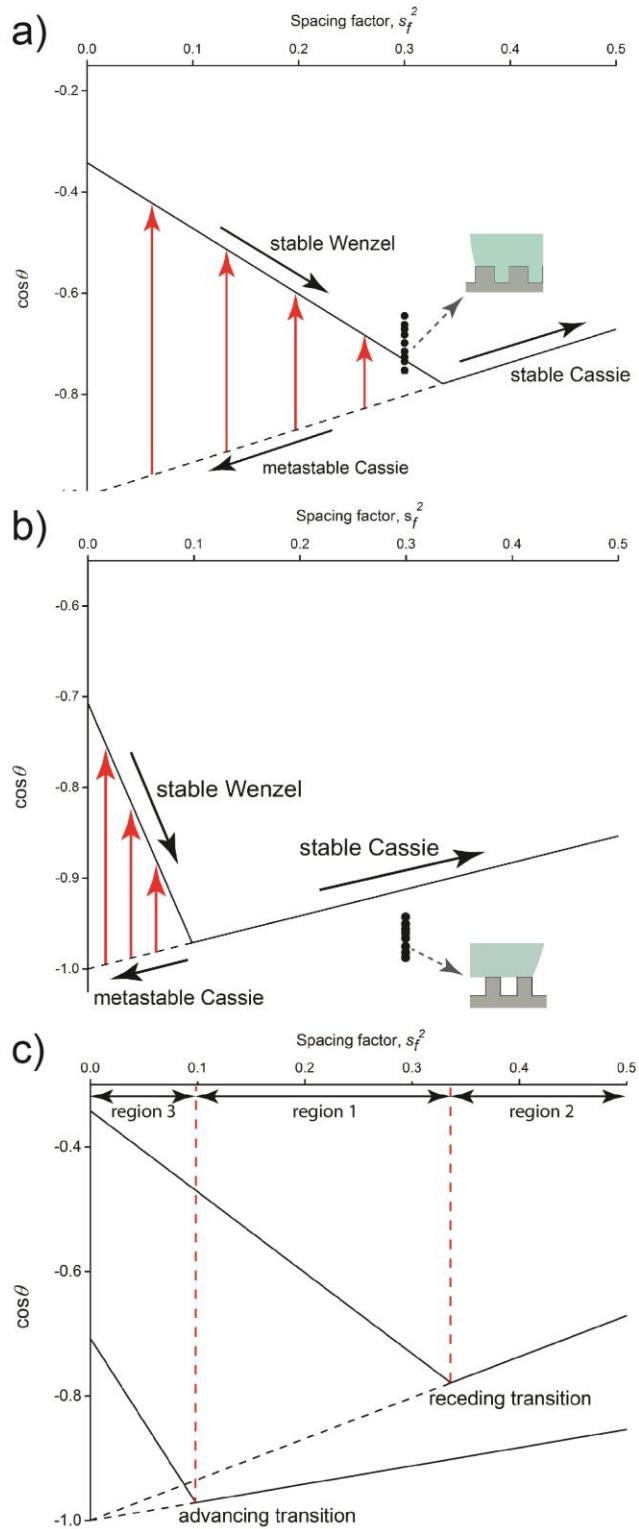
Figure 3.3. a) Transition between the Wenzel and Cassie–Baxter regimes on one-tier samples for the receding case ($\theta_{0,\mathrm{rec}} = 110°$). The receding transition occurs at $s_f{}^2 = 0.34$. b) Transition between the Wenzel and Cassie–Baxter regimes on one-tier

samples for the advancing case ($\theta_{0,\text{adv}} = 135°$). The advancing transition occurs at $s_f^2 =$ 0.098. c) Analysis of the Cassie to Wenzel transition over a wide range of the spacing factor s_f on one-tier surfaces. Black circles indicate the experimental values.

Thus, on the advancing frontier, contact zone stays on top of the micropillars and the Cassie–Baxter movement results in an easier motion of the advancing zone on one-tier surfaces. The conclusions drawn by the Wenzel-Cassie transition analysis (based on equations 3.6 and 3.7) are in good agreement with the experimental results on both advancing and receding contact zones on one-tier surfaces.

As can be seen in Fig. 3.3a and 3.3b, the (stable) Cassie state to the (stable) Wenzel state transition would eventually take place by continuously decreasing s_f^2, which means that reducing the pillars width a_m while increasing the pitch size p_m can ultimately transform a Cassie droplet to a Wenzel droplet. According to Fig. 3.3a and 3.3b, the transition from the (stable) Cassie regime to the (stable) Wenzel regime in the advancing case occurs at a smaller value of s_f^2 than in the receding case. The critical values of s_f^2 for the advancing and receding Cassie-Wenzel transitions on one-tier surfaces are 0.098 and 0.34, respectively, which indicates that Cassie state is the more favorable mode in the advancing zone. The receding movement follows the Wenzel mode up to a larger value of $s_f^2 = 0.34$. Consequently, on micropillars with $0.098 < s_f^2 <$ 0.34, the droplet receding contact zone motion remains sticky. Fig. 3.3c is the overview of both the advancing and receding transitions on one-tier samples. The transition diagrams are divided into three regions to better investigate the dynamic behavior of water droplets over a wide range of spacing factors.

1. Region 1: $0.098 < s_f^2 < 0.34$

In this region, the advancing zone stays in the Cassie regime while the receding zone follows the Wenzel behavior. Therefore, the advancing and receding governing equations in this region would be

$$\cos\theta_{adv} = s_f^2\left(\cos\theta_{0,adv} + 1\right) - 1 = s_f^2(\cos 135 + 1) - 1 = 0.2929 s_f^2 - 1 \qquad (3.8)$$

$$\cos\theta_{rec} = \left(1 + 3.8 s_f^2\right)\cos\theta_{0,rec} = \left(1 + 3.8 s_f^2\right)\cos 110 = -1.299 s_f^2 - 0.342 \qquad (3.9)$$

It is noteworthy that contact line/zone motion involves three phase interfaces: liquid-vapor (LV), solid-vapor (SV), and solid-liquid (SL). In the vicinity of the advancing zone, liquid particles on the liquid-vapor interface advance towards the rough structures (attach). In contrast, near the receding contact zone liquid particles detach from the rough structures as the droplet recedes. Assuming *dx* is an infinitesimal displacement in the direction of the contact line movement, the infinitesimal interfacial energy change *dE* of the advancing frontier would be proportional to $-\gamma_{LV} dx(1 + cos\theta)$ as the liquid-vapor and solid-vapor interfaces merge to a solid-liquid interface ($LV + SV \rightarrow SL$). Hence, for a dynamic droplet on a rough substrate, the total interfacial energy on the advancing contact zone decreases. Owing to the reduction in total interfacial energy, the advancing movement is considered as a spontaneous motion. The following energy analysis demonstrates a decrease in total interfacial energy of the advancing contact zone. As mentioned before, on the advancing frontier: $LV + SV \rightarrow SL$. In the following discussion, the interfacial energy difference between the right hand side (E_2: SL interface) and left hand side (E_1: LV+SV) of the stated relation ($LV + SV \rightarrow SL$) will be derived and calculated.

$$E_1 = adx(\gamma_{LV} + \gamma_{SV}) \qquad (3.10)$$

$$E_2 = adx(\gamma_{SL}) \qquad (3.11)$$

Where *a* is the width of the micropillars and *dx* is an infinitesimal element in the direction of the advancing movement (Assume that the droplet is moving along x direction). Now the total infinitesimal interfacial energy change for the advancing movement can be calculated:

$$\Delta E = E_2 - E_1 = adx(\gamma_{SL} - (\gamma_{LV} + \gamma_{SV})) \tag{3.12}$$

By dividing the right and left hand sides of the above equation to γ_{LV}:

$$\frac{\Delta E}{\gamma_{LV}} = -adx(1 + \frac{\gamma_{SV} - \gamma_{SL}}{\gamma_{LV}}) \tag{3.13}$$

Young's equation can be applied to simplify the above equation. According to Young's equation, there is a relationship between the contact angle and the surface tensions of the SV, SL, and LV interfaces (Young's equation: $cos\theta = \frac{\gamma_{SV} - \gamma_{SL}}{\gamma_{LV}}$). By combining the Young's equation with equation 3.13:

$$\frac{\Delta E}{\gamma_{LV}} = -adx(1 + cos\theta) \rightarrow \Delta E = -a\gamma_{LV}dx(1 + cos\theta) \tag{3.14}$$

The right hand side of equation 3.14 is negative ($0 < 1 + cos\theta < 2$ and *a, dx*, and γ_{LV} have positive values). Therefore, ΔE for the advancing motion is negative. Owing to the decrease in total interfacial energy on the advancing contact line, the advancing movement occurs spontaneously. A comparison between apparent advancing contact angles on one-tier surfaces with intrinsic advancing contact angle on the smooth substrate leads us to the same conclusion. The top of the micropillars is considered as a smooth (flat) surface, which exhibits $\theta_{0,adv}$= 135°. However, in macroscopic scale droplets on micropillars exhibit higher apparent advancing contact angles (~170°). Thus, forward movement of the advancing contact line occurs spontaneously. The spontaneous motion of the advancing contact line leads the liquid particles in the vicinity

of the advancing zone to roll as the droplet moves on the micropillars. This phenomenon is called the rolling mechanism [22] of the advancing zone and is illustrated in Fig. 3.4a. The rolling of the advancing contact zone leads to the Cassie-type behavior over the interval $0.098 < s_f^2 < 0.34$. Therefore, the rolling mechanism facilitates the advancing movement with less viscous dissipation than the receding motion. Nevertheless, in the receding edge, total interfacial energy increases since the solid-liquid interface splits into liquid-vapor and solid-vapor interfaces ($\mathrm{SL} \rightarrow \mathrm{LV} + \mathrm{SV}$). The total infinitesimal interfacial energy change for the receding case is:

$$\Delta E = a\gamma_{LV}dx(1 + cos\theta) \tag{3.15}$$

The process of deriving this relation is similar to equation 3.14. The only difference is a negative sign due to the opposite direction of the interface conversions. It can be clearly seen that ΔE for the receding movement has a positive value. As a result, the receding motion is not thermodynamically favorable. In this interval ($0.098 < s_f^2 < 0.34$), the receding movement follows the Wenzel behavior with liquid filling up the cavities between the micropillars (Fig. 3.4b). Therefore, in the receding event the droplet is in contact with not only the top of the micropillars but also the cavity surfaces between the surface asperities (the black-shaded area), which leads to remarkable pinning of the receding contact zone in this interval. Hence, to make the droplet recede, the liquid particles slightly above this shaded zone must move upward and detach from the shaded areas. The pinning of the receding contact zone can be also described from contact angle point of view. The intrinsic receding contact angle on top of or between the smooth micropillars (110°) is lower than the macroscopic (apparent) receding contact angles on one-tier samples (~134°). Thus, as illustrated in Fig. 3.4b, the

receding contact zone adheres to the micropillars unless liquid particles at the receding

zone detach from the black shaded area and jump to the next (red) shaded area. The

strong receding contact line pinning accounts for the sticky behaviors of the receding

contact zone over the interval of $0.098 < s_f^2 < 0.34$. Therefore, the significant contact

angle hysteresis on one-tier samples is attributed to the pinning of the receding contact

line. Gao and McCarthy [30] also ascribed the high contact angle hysteresis 29⁰ on their

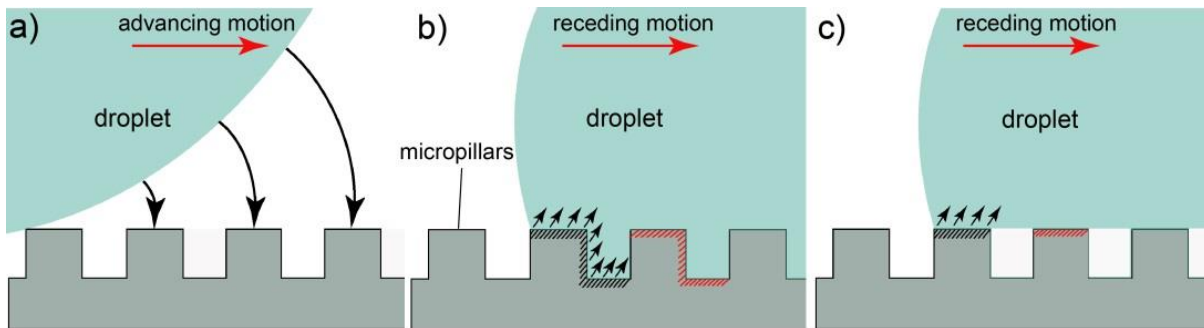micropatterned samples to the noticeable pinning of the receding contact zone.

Figure 3.4. a) The rolling mechanism of the advancing contact line/zone. b) The remarkable pinning of the receding contact line/zone corresponding to the Wenzel state. c) The relatively moderate pinning of the receding contact line/zone corresponding to the Cassie state.

In region 1, there is a high tendency for the advancing zone to be in the Cassie

state as the rolling mechanism dominates the advancing movement. On the other hand,

the pinning of the receding contact line plays an important role in explaining the sticky

behavior of the receding motion. Independent of the roughness geometry (height, pitch,

etc), the rolling mechanism keeps the advancing motions in Cassie state over the

interval of $0.098 < s_f^2 < 0.34$. Fig. 3.5 illustrates the dynamic behavior of the advancing

and receding contact lines on the one-tier surface with $0.098 < s_f^2 < 0.34$.
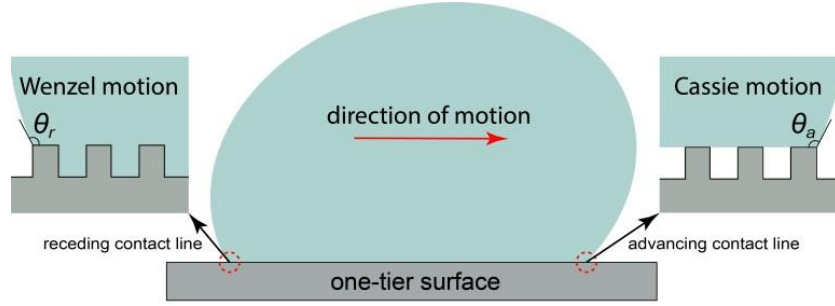
Figure 3.5. Dynamic behavior of the advancing and receding contact lines on the one-tier surface with $0.098 < s_f{}^2 < 0.34$.

2. Region 2: $s_f^2 > 0.34$

In this interval both the advancing and receding contact zones follow the Cassie–Baxter model. The corresponding equations for advancing and receding lines in region 2 would be:

$$\cos\theta_{adv} = s_f^2(\cos\theta_{0,adv} + 1) - 1 = s_f^2(\cos135 + 1) - 1 = 0.2929 s_f^2 - 1 \qquad (3.16)$$

$$\cos\theta_{rec} = s_f^2(\cos\theta_{0,rec} + 1) - 1 = s_f^2(\cos110 + 1) - 1 = 0.658 s_f^2 - 1 \qquad (3.17)$$

Increasing the micropillar width a_m while decreasing the pitch size p_m makes the droplet preferably stay on top of the micropillars in both the advancing and receding events. During the receding motion the receding edge disjoins from the micropillar tips and jumps to the top of the next neighboring micropillar. Owing to the considerable decrease in the liquid-solid contact area (shaded zone in Fig. 3.4c) the pinning of the receding contact zone has a significantly less effect in this region. Thus, sticky behaviors are greatly alleviated in the receding zone in region 2. On the advancing frontier, the rolling mechanism still keeps the advancing zone in the Cassie mode.

3. Region 3: $s_f^2 < 0.098$

In this interval, both the advancing and receding movements are predicted to follow the Wenzel model. Droplet staying on top of the micropillars becomes

unfavorable when the spacing factor s_f^2 is below the critical value 0.098. Increasing the

pitch size p_m with a decrease in the width of the micropillars a_m eventually leads the

advancing contact zone to the Wenzel regime. As a result, sticky behaviors are

expected on both the advancing and receding edges in region 3. The governing

equations for the Wenzel and Cassie-Baxter line in this region would be

$$\cos\theta_{adv} = (1 + 3.8s_f^2)\cos\theta_{0,adv} = (1 + 3.8s_f^2)\cos135 = -2.687s_f^2 - 0.707 \quad (3.18)$$

$$\cos\theta_{rec} = (1 + 3.8s_f^2)\cos\theta_{0,rec} = (1 + 3.8s_f^2)\cos110 = -1.299s_f^2 - 0.342 \quad (3.19)$$

The following table summarizes the relationship between $\cos\theta$ and s_f^2 for different

intervals of the spacing factor on both advancing and receding events.

Table 1

Comparison of the advancing/receding governing equations between different regions
of the spacing factor

| region	advancing governing equation	receding governing equation
region 1 $(0.098 < s_f^2 < 0.34)$	$\cos\theta_{adv} = 0.2929s_f^2 - 1$	$\cos\theta_{rec} = -1.299s_f^2 - 0.342$
region 2 $(s_f^2 > 0.34)$	$\cos\theta_{adv} = 0.2929s_f^2 - 1$	$\cos\theta_{rec} = 0.658s_f^2 - 1$
region 3 $(s_f^2 < 0.098)$	$\cos\theta_{adv} = -2.687s_f^2 - 0.707$	$\cos\theta_{rec} = -1.299s_f^2 - 0.342$

CHAPTER 4

CONTACT LINE OSCILLATIONS

As described in the previous chapter, the receding motion on one-tier samples

exhibit significant contact line pinning. The pinning/de-pinning behavior of the receding

contact line leads to remarkable contact angle oscillations on the receding event. In this

chapter, the author experimentally investigates contact angle fluctuations of both

advancing and receding movements during droplet transport. It is noteworthy that the

fluctuations are not only limited to the contact angles. The fluctuations of the (advancing

or receding) contact line velocities are to be also taken into account. Hence, the

oscillations have been also studied for both advancing and receding contact line

velocities. In order to study the effects of surface roughness on contact line oscillations,

the author has carried out the experimental analysis for smooth, one-tier (with Si

micropillars), and two-tier (with CNTs grown on Si micropillars) surfaces. In order to

accurately analyze contact line fluctuations, the recorded movies is utilized to analyze

the advancing and receding contact angles/velocities fluctuations with time step of

$\Delta t = 0.05 s$ on all three types of surfaces. In this way, the researcher could gain a firm

understanding on the effects of surface roughness on contact line oscillations.

4.1 Contact Line Oscillations on the One-tier Surface

The experimental results demonstrate that on one-tier structure remarkable

fluctuations is observed owing to the strong contact line pinning of the receding

movement. However, the fluctuations are much smaller on the advancing movement. As

mentioned in the previous chapter, the rolling mechanism facilitates the advancing

motion on the one-tier surface. As a result, on the advancing movement, smaller

fluctuations are observed in comparison with the receding motion. Furthermore, the

energy analysis demonstrates that advancing movement is more favorable since the

total energy decreases upon advancing motion. Therefore, oscillations on the receding

movement are expected to have significantly larger amounts than the advancing

movement. Fig. 4.1 demonstrates the significant fluctuations on the receding contact
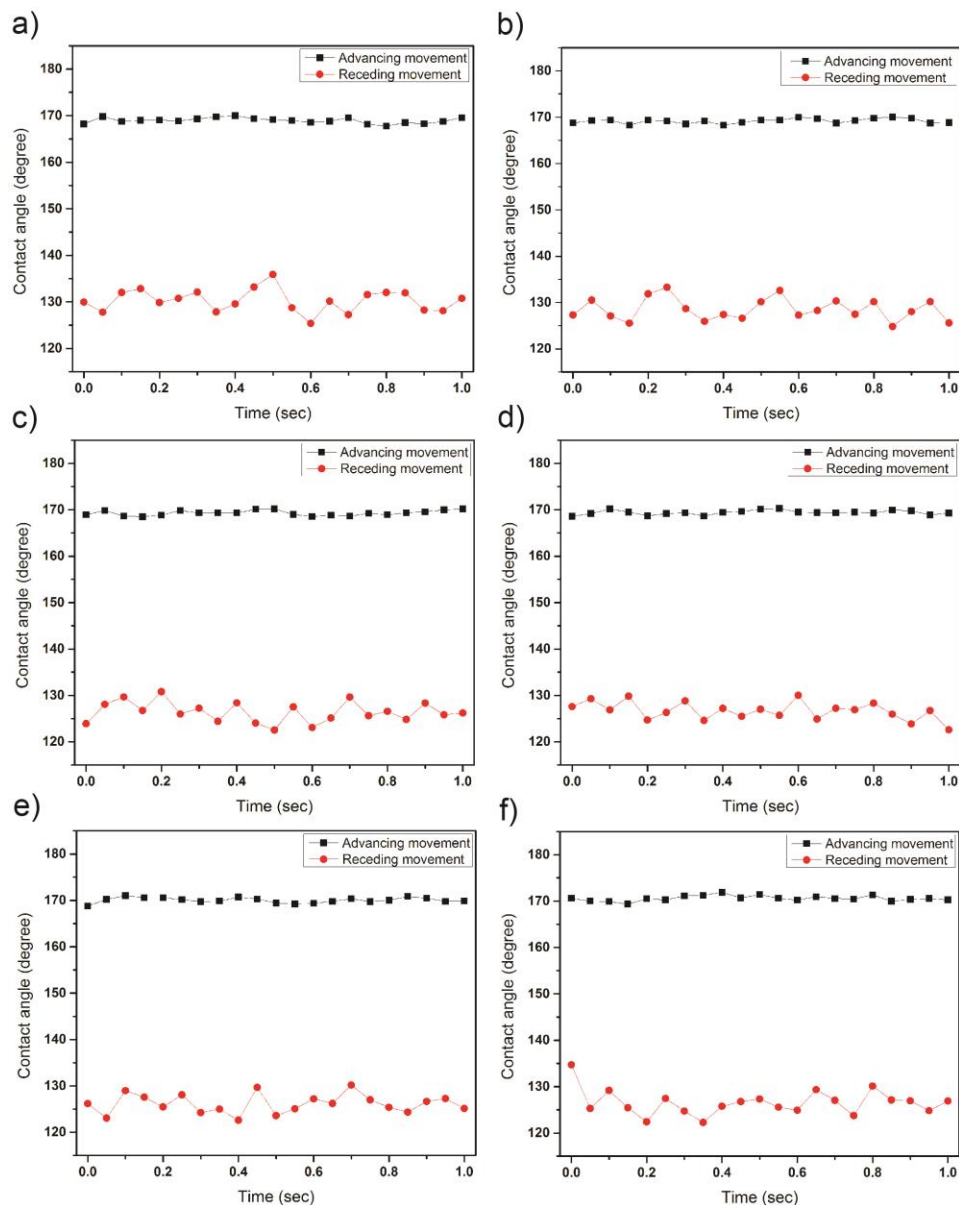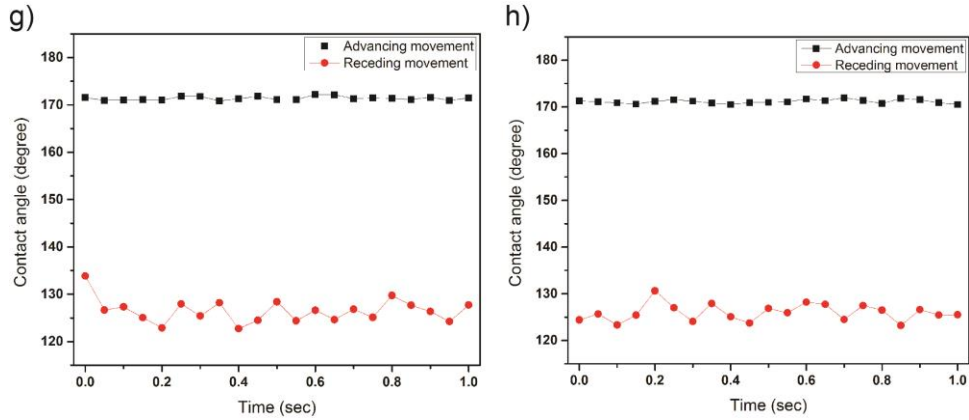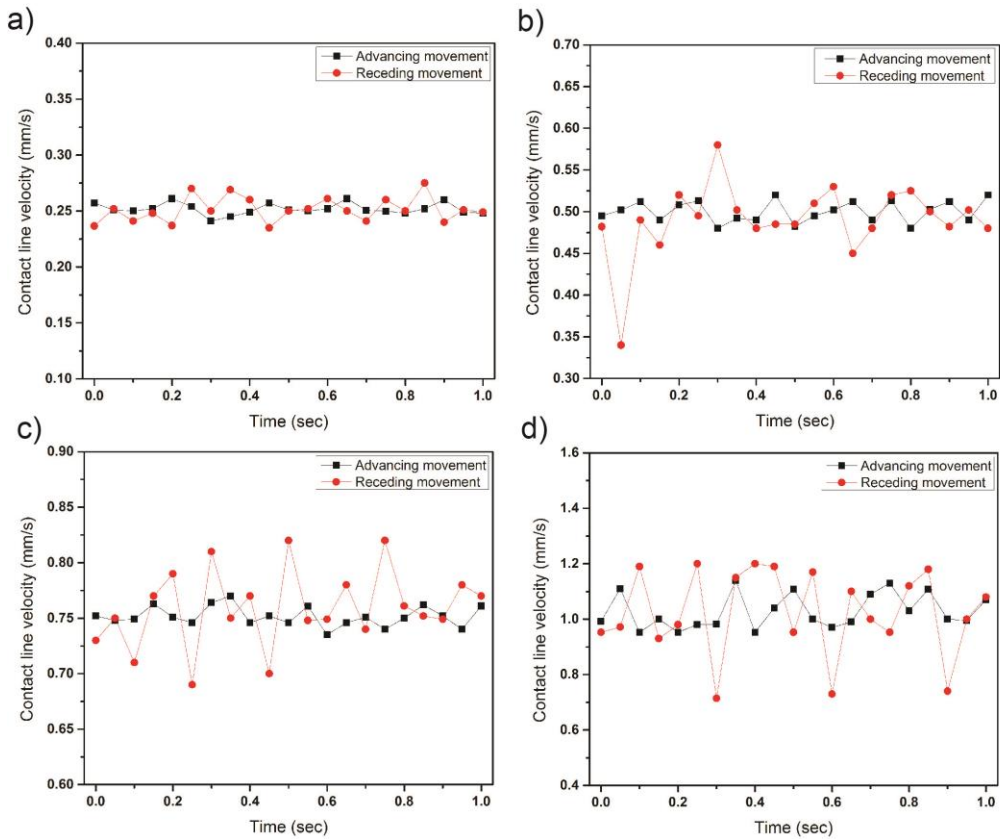
angle.

Figure 4.1. Advancing and receding contact angle fluctuations over time on the one-tier surface for the droplet velocity of a) 0.25 mm/s, b) 0.5 mm/s, c) 0.75 mm/s, d) 1 e)1.5 mm/s, f) 2 mm/s, g)2.5 mm/s, and h) 3 mm/s.

Fig. 4.2 displays the oscillations of the contact line velocity over time during the droplet movement on the one-tier surface.
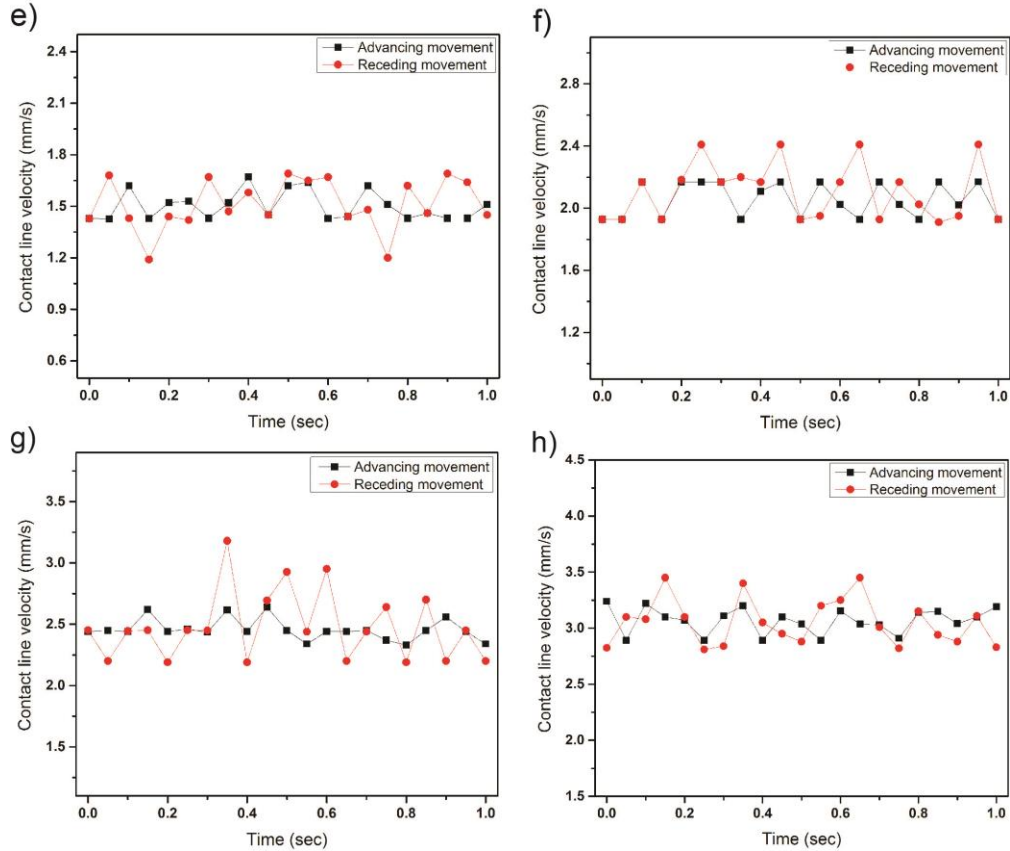
Figure 4.2. Advancing and receding contact line velocity fluctuations over time on the one-tier surface for the droplet velocity of a) 0.25 mm/s, b) 0.5 mm/s, c) 0.75 mm/s, d) 1 mm/s, e)1.5 mm/s, f) 2 mm/s, g) 2.5 mm/s, and h) 3 mm/s.

As can be seen in Fig. 4.2, the receding contact line velocity on one-tier samples exhibit remarked fluctuations while the advancing velocities show much less changes during droplet motion.

4.2 Contact Line Oscillations on the Smooth Surface

It is noteworthy that the contact angle/velocity oscillations on the smooth surface have less amounts than the one-tier surface (Fig. 4.3).
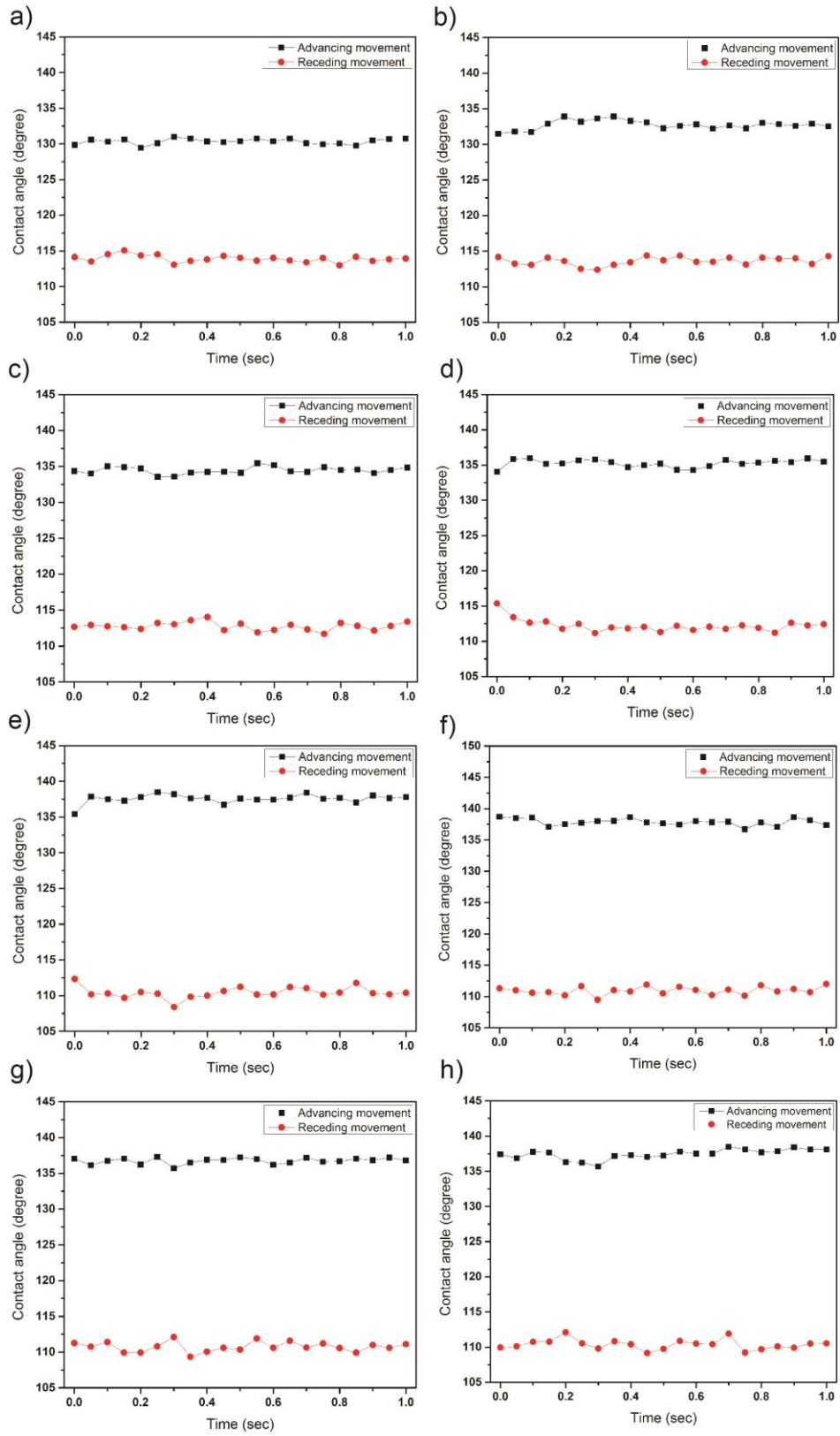
The smooth surface is perfectly polished and there is no surface roughness on it. Due to the absence of any asperities on smooth surface, the contact angle/velocity oscillations are considerably smaller than the one-tier structure. Fig. 4.3 illustrates the advancing and receding contact angle fluctuations on the smooth surface during droplet motion. Similar to the one-tier surface, the oscillations of the advancing and receding contact line velocities during the droplet movement on the smooth surface have been measured. As can be seen in Fig. 4.4, both advancing and receding fluctuations exhibit slight fluctuations. This is due to the absence of surface roughness on the smooth substrate.
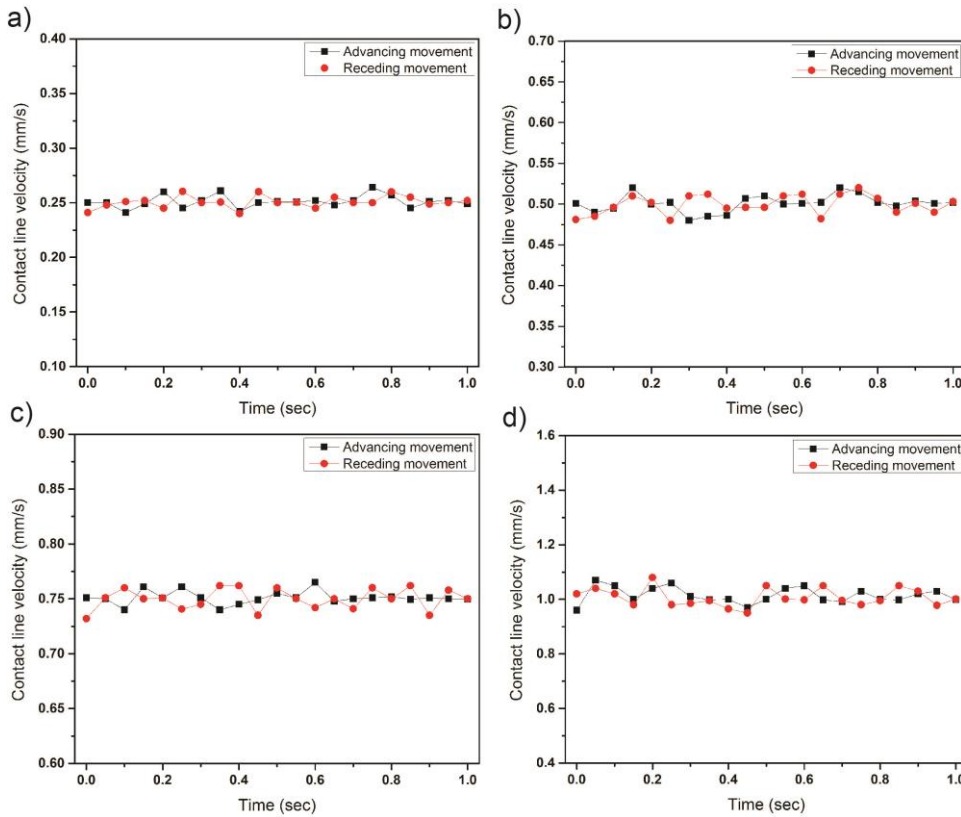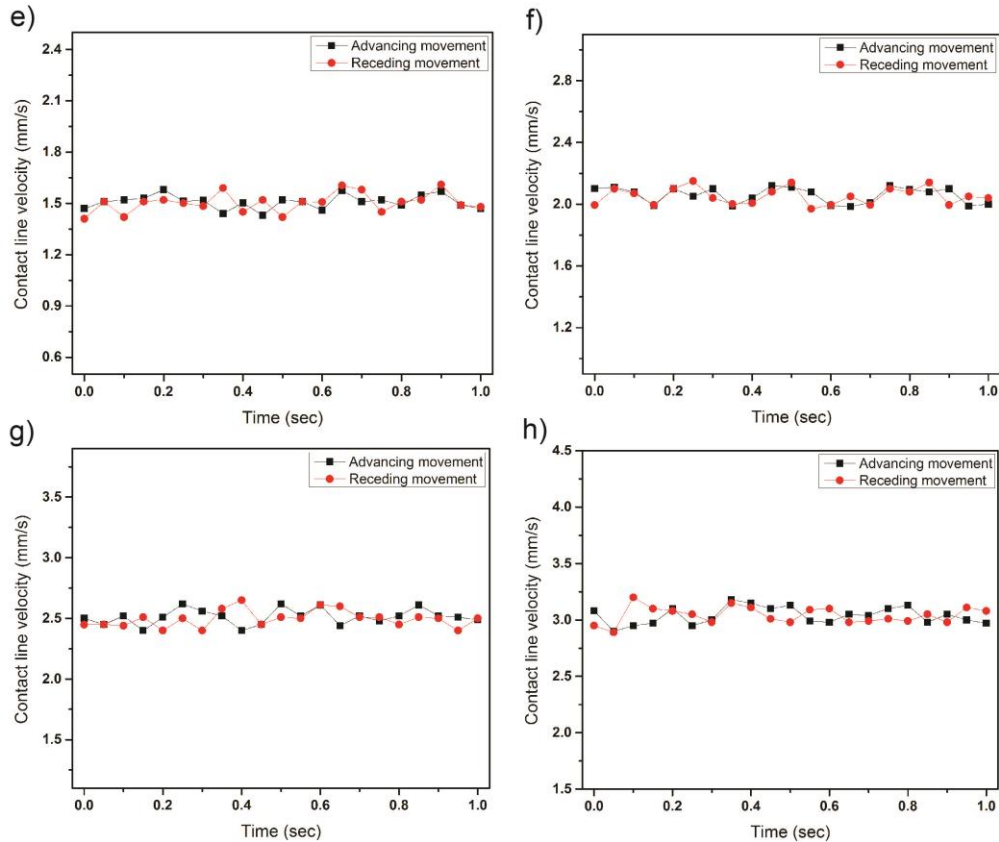
Figure 4.4. Advancing and receding contact line velocity fluctuations over time on the smooth surface for the droplet velocity of a) 0.25 mm/s, b) 0.5 mm/s, c) 0.75 mm/s, d) 1 mm/s, e)1.5 mm/s, f) 2 mm/s, g) 2.5 mm/s, and h) 3 mm/s.

4.3 Contact Line Oscillations on the Two-tier Surface

The provided results indicate that superhydrophobic surfaces with CNTs on top of micropillars can significantly decrease both the advancing and receding oscillations. This phenomenon can be explained by comparing the roughness geometry of the one-tier and two-tier structures. The following table summarizes the geometric properties of both one-tier and two-tier surfaces.

Table 2

Comparison of the Wenzel and Cassie–Baxter geometric parameters on the one-tier and two-tier structures

surface	r	f
one-tier	2.17	0.3
two-tier	6.51	0.06

The surface roughness r of the two-tier structure is significantly higher than that of the one-tier structure, i.e., 6.51 vs. 2.17. Moreover, the solid-liquid contact fraction f on the two-tier surface is 5 times smaller than that of the one-tier surface. This fact reveals that the wetted solid surface underneath the water droplet on the two-tier surface is substantially smaller than that on the one-tier surface. Hence, it is the Cassie–Baxter model that dominates the droplet transport (both advancing and receding) on the two-tier surface. That is why the contact angle fluctuations are extremely low on the two-tier structure (less than 1°). Fig. 4.5 validates the tiny oscillations of the advancing and receding contact angles on the two-tier substrate for different velocities of water droplet.
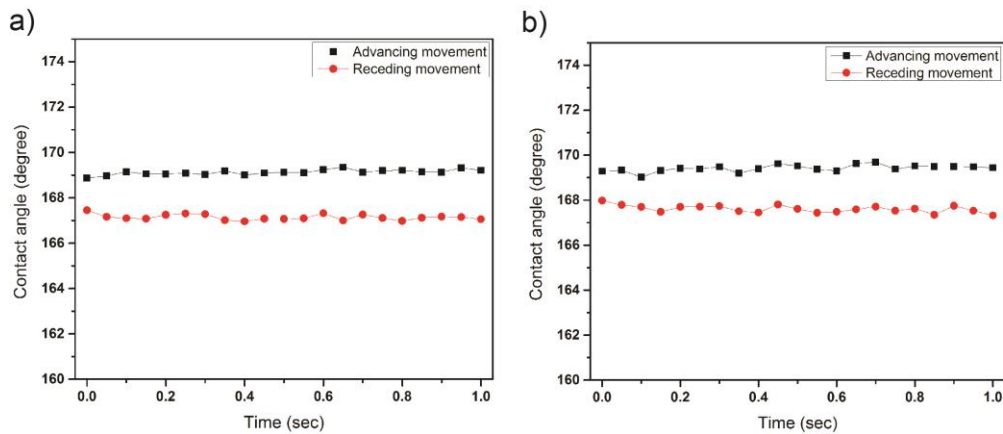
Figure 4.5. Advancing and receding contact angle fluctuations over time on the two-tier surface for the droplet velocity of a) 0.25 mm/s, b) 0.5 mm/s, c) 0.75 mm/s, d) 1 mm/s, e)1.5 mm/s, f) 2 mm/s, g) 2.5 mm/s, and h) 3 mm/s.

Standing on top of asperities facilitates the droplet motion which leads to really small fluctuations on the two-tier substrate. Fig. 4.6 illustrates the fluctuations of the contact line velocity on the two-tier surface. As can be clearly seen, the combination of
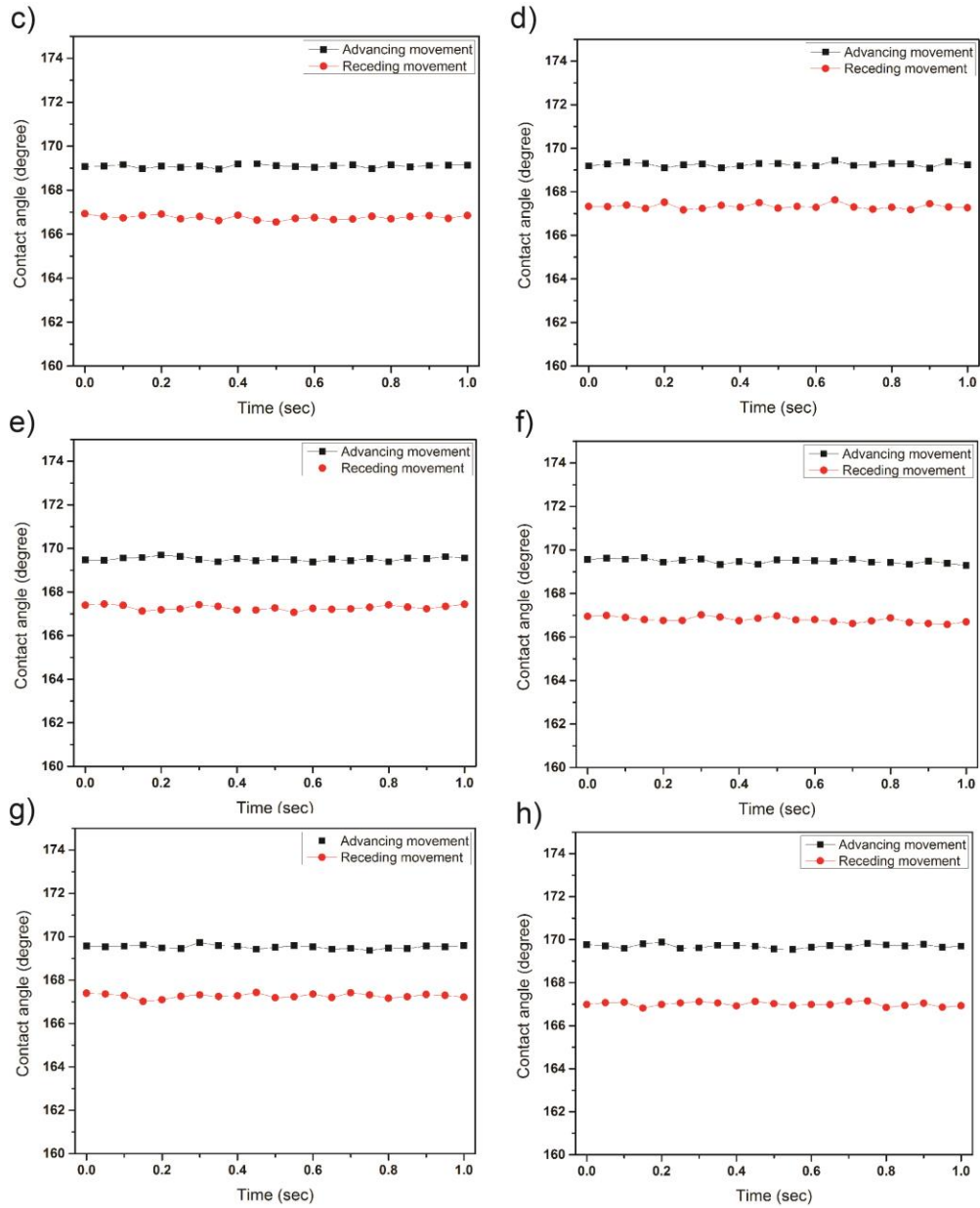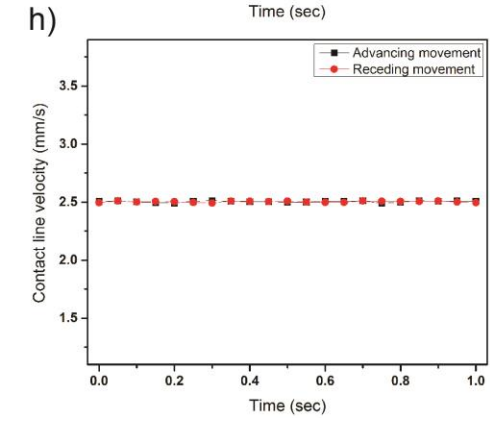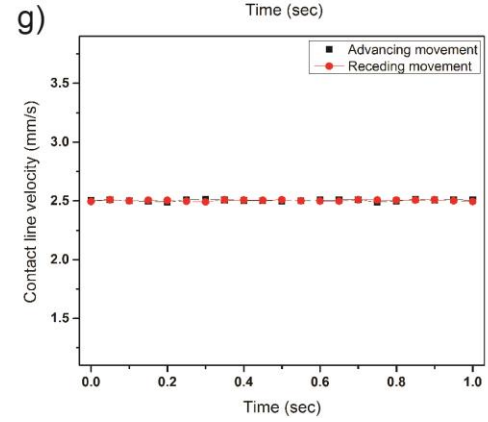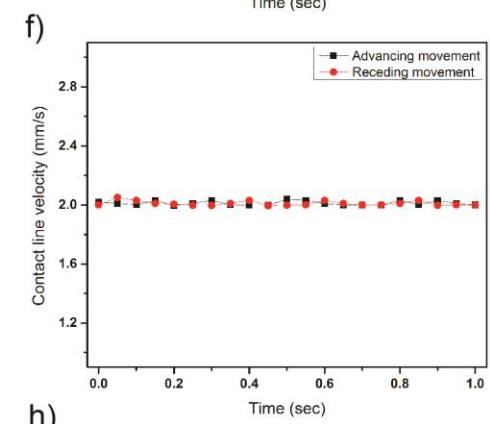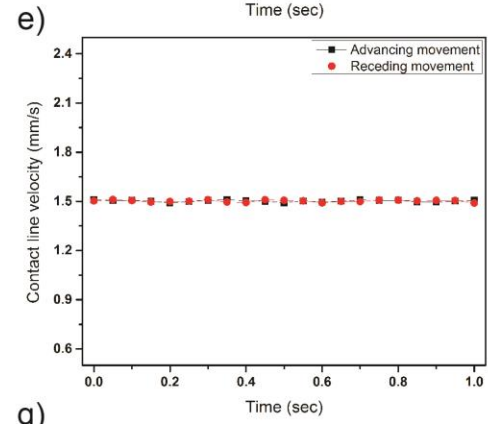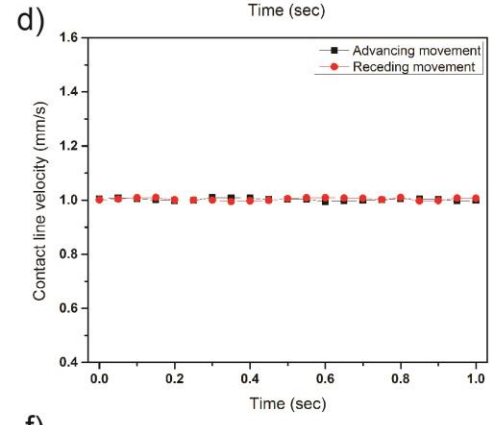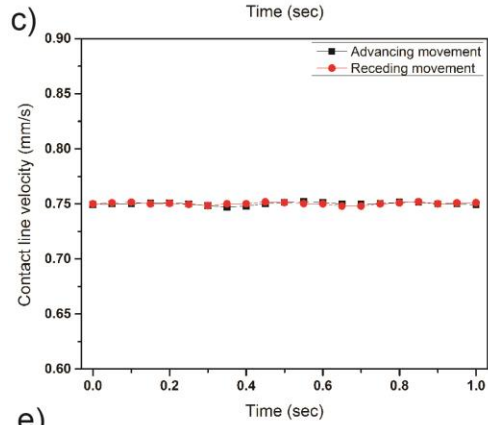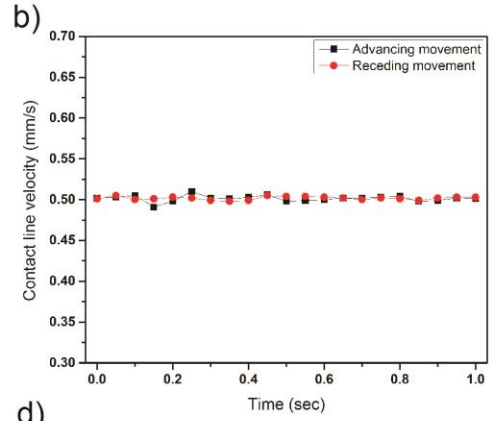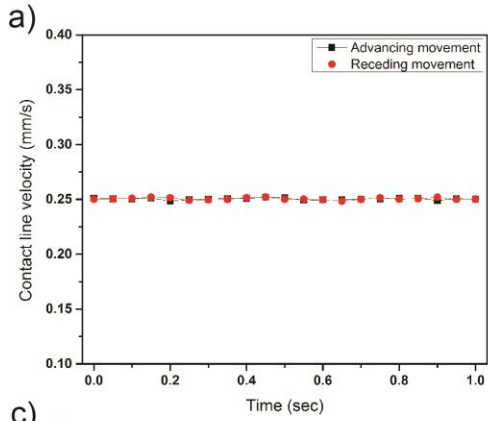
Figure 4.6. Advancing and receding contact contact line velocity fluctuations over time on the two-tier surface for the droplet velocity of a) 0.25 mm/s, b) 0.5 mm/s, c) 0.75 d) 1 mm/s, e)1.5 mm/s, f) 2 mm/s, g) 2.5 mm/s, and h) 3 mm/s.

micro and nano structures on the two-tier substrate can significantly enhance the droplet transport. For the sake of comparison, fluctuations of a 15 μl droplet on the smooth, one-tier, and two-tier surfaces have been plotted in the same diagram (In all cases the moving stage velocity is 0.75 mm/s). Fig. 4.7 compares contact line oscillations on smooth, one-tier, and two-tier substrates. Fig. 4.7a and 4.7b correspond to the advancing contact angles and advancing contact line velocities respectively and Fig. 4.7c and 4.7d represent the receding contact angles and receding contact line velocities respectively.
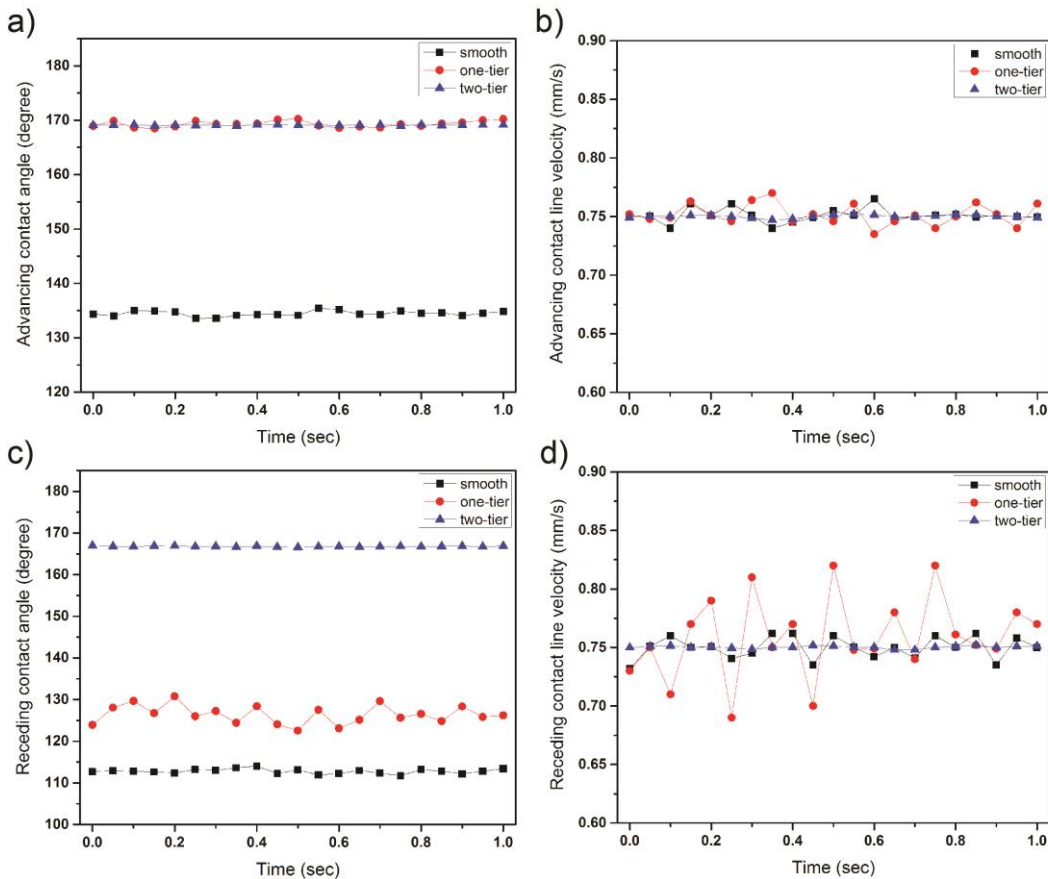
Figure 4.7. Comparison of the smooth, one-tier, and two-tier oscillations on a) advancing contact angle, b) advancing contact line velocity, c) receding contact angle, and d) receding contact line velocity. The droplet volume is $15\mu l$ and it is moving at 0.75 mm/s.

As can be seen, the fluctuations of the receding contact line on the one-tier surface are remarkable. Fig. 4.7c demonstrates the significant oscillation of the receding contact angle on the one-tier substrate in comparison with the smooth and two-tier structures. Similarly, Fig. 4.7d portrays considerable fluctuations of the receding contact line velocity on the one-tier structure. This remarked fluctuation was attributed to the strong contact line pinning of the receding contact line on the one-tier surface. Moreover, as mentioned in the previous chapter, liquid particles in the vicinity of the receding contact line fills up the cavities between the micropillars (Wenzel model). Hence, due to the large contact area of the droplet and the solid surface the receding contact line movement becomes sticky which leads to significant contact angle/velocity oscillations on the one-tier surface. According to Fig. 4.7, two-tier substrate exhibit the lowest fluctuations on both advancing and receding events.

CHAPTER 5

CONTACT LINE FRICTION COEFFICIENT

In this chapter the author reports the effects of surface roughness on contact line friction coefficients (CLFCs) of water droplets on micro- and nano-patterned surfaces. Both advancing and receding CLFCs have been measured, analyzed and compared on smooth, one-tier (with micropillars), and two-tier (with carbon nanotubes (CNTs) grown on micropillars) surfaces over a wide range of contact line velocities and droplet volumes. The results indicate that superhydrophobic surfaces with CNTs on top of micropillars can significantly decrease both the advancing and receding CLFCs. In comparison, both the advancing and receding CLFCs on smooth surfaces are >10 times larger than those on superhydrophobic surfaces. However, droplets on one-tier surfaces with only micropillars exhibit different dynamic behaviors in advancing and receding movements. In chapter 3 the author experimentally investigated the Cassie state to Wenzel state transition on micropillar structures and found that the receding movement of a droplet on micropillars is dominated by the Wenzel behavior with remarkable receding contact line pinning. This pinning effect leads to a higher receding CLFC on one-tier surfaces. However, rolling mechanism of liquid particles in the vicinity of the advancing contact zone controls the advancing motion of a droplet on micropillars. There is a high tendency for the advancing contact line to exhibit the Cassie-type behavior on one-tier surfaces and hence the advancing CLFC is considerably mitigated. On two-tier superhydrophobic surfaces, it is the Cassie–Baxter behavior that dominates both the advancing and receding contact line motions giving rise to less friction coefficients.

Voue et al. had analyzed the effect of alkyl chain length on CLFC of liquid droplets on self-assembled monolayers [31]. But few work has been done to measure CLFC on structured surfaces. In this work, the author aims to measure and analyze the CLFCs of water droplets on smooth, one-tier (with micropillars), and two-tier (with carbon nanotubes (CNTs) grown on micropillars) surfaces. The main objective is to investigate the influence of surface roughness on CLFC, which is defined by the following relation [29]:

$$\xi = \frac{\gamma|cos\theta_s - cos\theta_d|}{U_c} \tag{5.1}$$

where ξ is the contact line friction coefficient, U_c is the contact line velocity, γ is the surface tension of water with air, θ_s is the static contact angle, and θ_d is the dynamic contact angle. This relation was directly derived from the molecular kinetic theory (MKT) [32, 33]. MKT theory states that the out-of-balance surface tension force acting on the contact line zone is the driving force of the contact line movement ($F_w = \gamma(cos\theta_s - cos\theta_d)$). According to equation 5.1, determination of the CLFC highly relies on precise measurement of the static and dynamic contact angles. Higher differences between the static and dynamic contact angles lead to a larger CLFC; and a lower friction coefficient results from smaller differences between the static and dynamic contact angles. The term $|cos\theta_s - cos\theta_d|$ in equation 5.1 indicates that in this work the researcher only considers the absolute value of the difference between $cos\theta_s$ and $cos\theta_d$ and therefore, the advancing and receding CLFCs have the same signs.

The following discussion is devoted to the derivation of the contact line friction coefficient formula by applying molecular kinetic theory (MKT). This theory has been widely accepted and used to delineate the wetting characteristics of a liquid on a

surface. This theory focuses on the processes of attachment and detachment of liquid particles in the vicinity of advancing and receding movements (within the three-phase zone). Consequently, MKT approach relates the dynamic contact angle (θ_D) to the contact line velocity (U). Fig. 5.1 shows the dynamics of a moving contact line according to the molecular kinetic theory.
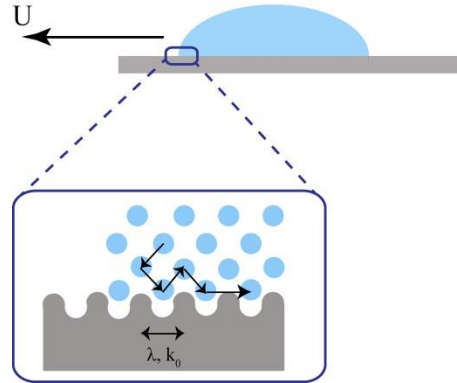
Figure 5.1. MKT theory.

According to this theory, the liquid particles are absorbed by the adsorption sites on the solid. k_0 is the equilibrium frequency of the random displacement of fluid molecules in the three-phase zone. λ is the average length of the molecular jumps. λ can also be defined as the average distance between the adsorption sites on the solid surface. K_0 has been derived as a function of molar activation energy ΔG_w^* as below [32]:

$$k_0 = (\frac{k_B T}{h}) \exp(\frac{-\Delta G_w^*}{N K_B T}) \tag{5.2}$$

where k_B, h, N, and T are Boltzmann constant, Planck constant, Avogadro number, and absolute temperature, respectively. k_0 is anisotropic in the proximity of the solid surface. If k^+ and k^- correspond to the advancing and receding movements respectively, the velocity of the contact line can be defined as:

$$v = \lambda(k^+ - k^-) \tag{5.3}$$

The contact line is stationary at equilibrium. Hence, one can state that the equilibrium frequency is isotropic:

$$k^+ = k^- = k_0 \tag{5.4}$$

When the equilibrium is disturbed, the frequencies will be imbalanced ($k^+ \neq k^-$) and as a result, the contact line will move in the direction of the greater frequency ($k^+ > k^-$). It is assumed that the out-of-balance surface tension force acting on the contact line can be considered as the driving force when the equilibrium is disturbed. Therefore, the contact line will move in the direction of this driving force (The same direction of k^+). The driving force (w) is defined as [33, 34]:

$$w = \gamma(cos\theta_s - cos\theta_d) \tag{5.5}$$

where θ_s and θ_d are the static and dynamic contact angles respectively. The following relations have been also derived for k^+ and k^- [32]:

$$k^+ = (\frac{k_B T}{h})\exp(\frac{-\Delta G_w^*}{NK_B T} + \frac{w}{2nK_B T}) \tag{5.6}$$

$$k^- = (\frac{k_B T}{h})\exp(\frac{-\Delta G_w^*}{NK_B T} - \frac{w}{2nK_B T}) \tag{5.7}$$

where n is the number of adsorption sites per unit area of the solid surface. By substituting equations 5.6 and 5.7 into equation 5.3:

$$v = \frac{k_B T \lambda}{h} \exp\left(\frac{-\Delta G_w^*}{NK_B T}\right) \left(\exp\left(\frac{w}{2nK_B T}\right) - \exp\left(\frac{-w}{2nK_B T}\right) \right) \tag{5.8}$$

Therefore,

$$v = 2\left[(\frac{k_B T}{h}) \exp\left(\frac{-\Delta G_w^*}{NK_B T}\right) \right] \lambda \sinh\left(\frac{w}{2nK_B T}\right) \tag{5.9}$$

By applying equation 5.2 on the above relation:

$$v = 2k_0\lambda\sinh\left(\frac{w}{2nK_BT}\right)$$

(5.10)

By substituting equation 5.5 into equation 5.10:

$$v = 2k_0\lambda\sinh\left(\frac{\gamma(cos\theta_s - cos\theta_d)}{2nK_BT}\right)$$

(5.11)

n, the number of adsorption sites per unit area, can be approximated by λ^{-2}. This

approximation is based upon the assumption that the adsorption sites are distributed

uniformly on the solid surface. Hence, equation 5.11 can be rewritten as:

$$v = 2k_0\lambda\sinh\left(\frac{\gamma(cos\theta_s - cos\theta_d)\lambda^2}{2K_BT}\right)$$

(5.12)

Several authors have applied equations 5.11 and 5.12 in their works: M. J. De Ruijter et

al. [32], T. D. Blake [33], H. B. Eral et al. [34], and R.A. Hayes [35].

The Taylor series expansion of the function sinh x is as below:

$$\sinh x = x + \frac{x^3}{3!} + \frac{x^5}{5!} + \frac{x^7}{7!} + \cdots$$

(5.13)

Hence, for small values of x:

$$\sinh x \sim x$$

(5.14)

The term $\frac{\gamma(cos\theta_s - cos\theta_d)\lambda^2}{2K_BT}$ in the equation 5.12 is a small number. Hence, the term

$\sinh\left(\frac{\gamma(cos\theta_s - cos\theta_d)\lambda^2}{2K_BT}\right)$ can be approximated by $\frac{\gamma(cos\theta_s - cos\theta_d)\lambda^2}{2K_BT}$. Therefore, equation 5.12

can be linearized as:

$$v = 2k_0\lambda\left(\frac{\gamma(cos\theta_s - cos\theta_d)\lambda^2}{2K_BT}\right)$$

(5.15)

or

$$v = \frac{k_0\lambda^3}{K_BT}\left(\gamma(cos\theta_s - cos\theta_d)\right)$$

(5.16)

The term $\frac{K_B T}{k_0 \lambda^3}$ or $\frac{n K_B T}{k_0 \lambda}$ is also called the friction coefficient of the contact line (ξ_0). Hence, equation 5.16 can be rewritten as:

$$v = \frac{1}{\xi_0} \gamma (cos\theta_s - cos\theta_d) \tag{5.17}$$

Therefore, the contact line friction coefficient can be expressed as:

$$\xi_0 = \frac{\gamma (cos\theta_s - cos\theta_d)}{v} \tag{5.18}$$

This relation has been repeatedly used in the literature [32-34]. In this work, the author used this formula to calculate the contact line friction coefficient of water droplets on the samples. (As noted before, the term $|cos\theta_s - cos\theta_d|$ in equation 5.1 indicates that in this work the absolute value of the difference between $cos\theta_s$ and $cos\theta_d$ is only considered and therefore the advancing and receding contact line friction coefficients have the same signs). Therefore, the final formula for calculating the contact line friction coefficient is:

$$\xi = \frac{\gamma |cos\theta_s - cos\theta_d|}{U_c} \tag{5.19}$$

Fig. 5.2a and 5.2b plot the advancing and receding CLFCs of a water droplet of 25 μl versus the advancing and receding contact line velocities, respectively, on smooth, one-tier, and two-tier surfaces. At relatively lower contact line velocities, CLFC decreases with increasing droplet speed (and hence contact line velocity). But the friction coefficient reaches an approximately constant value at higher contact line velocities. In this study, this saturated value is considered as the CLFC. As shown in Fig. 5.2a, advancing CLFCs on different surfaces have the following relationship:

$$\xi_{adv-smooth} > \xi_{adv-one-tier} > \xi_{adv-two-tier} \tag{5.20}$$

In the advancing case, it seems that a higher degree of surface roughness and a smaller solid fraction factor lead to a lower CLFC. The surface roughness r_m of the one-tier sample is lower than the surface roughness $r_m r_n$ of the two-tier surface but larger than the smooth surface. Hence, the advancing CLFCs on the one-tier surface are larger than the corresponding values of the two-tier surface but are smaller than those values on the smooth surface.

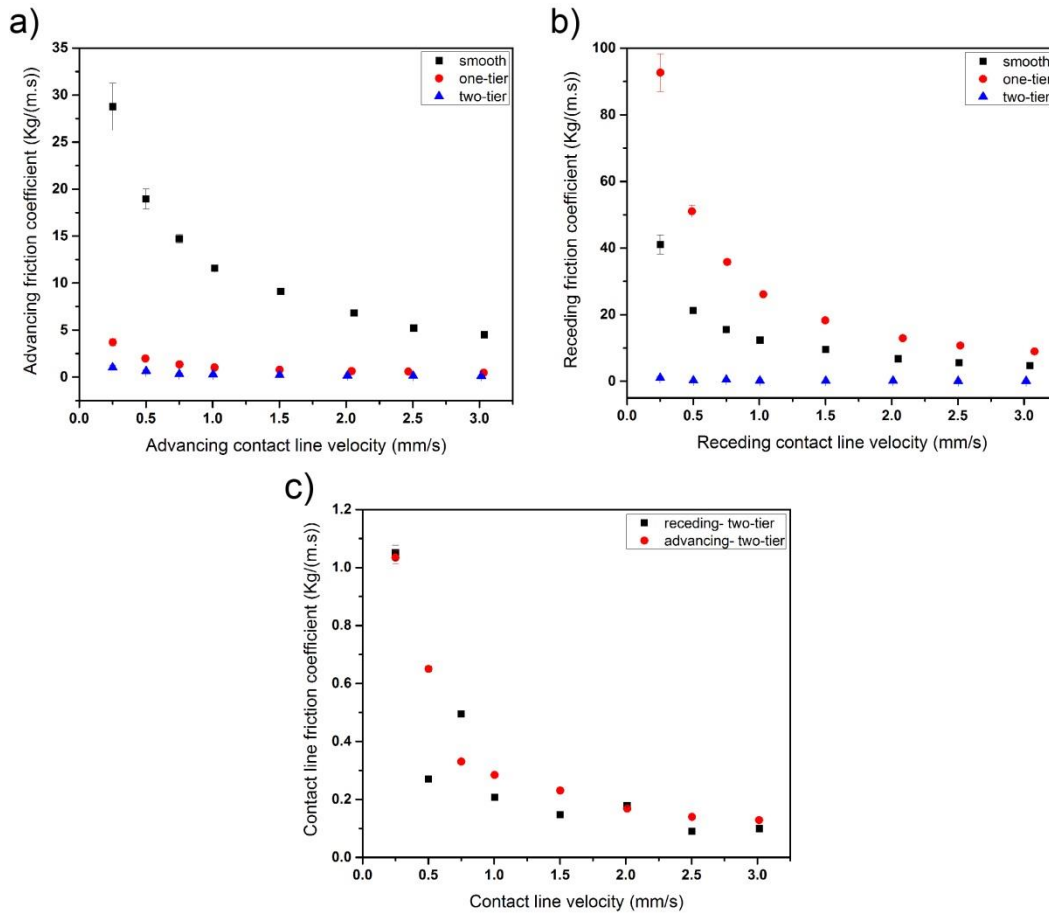*Figure 5.2.* a) Comparison of the advancing CLFCs on different surfaces, b) Comparison of the receding CLFCs on different surfaces, c) Illustration of the CLFCs versus contact line velocity on the two-tier texture with a proper scaling. In all cases the droplet volume is 25 *μl*.

Fig. 5.2b compares the receding CLFCs on the three surfaces. The friction coefficients in the receding zone are found to follow:

$$\xi_{\text{rec-one-tier}} > \xi_{\text{rec-smooth}} > \xi_{\text{rec-two-tier}} \tag{5.21}$$

The receding CLFCs on the smooth surface are larger than the corresponding values of the two-tier surface but are smaller than the coefficients of the one-tier surface. Unlike the advancing case, the receding CLFC on the one-tier surface has the highest value. This is due to the significant changes in the dynamic receding contact angle on the one-tier surface. The experiments on the one-tier surface show that the difference between the static and dynamic contact angles on the advancing frontier is considerably low (~2° to 6.5°), but the corresponding difference at the receding edge ranges from 26° to 41°. As a result, the one-tier surface has the highest receding CLFC.

Fig. 5.2a and 5.2b indicate that the two-tier surface has the lowest CLFCs on both the advancing frontier and the receding edge, which result from the extremely low differences between the static and dynamic contact angles. For the sake of illustration, both advancing and receding CLFCs on the two-tier structure are shown in Fig. 5.2c with a proper scaling. Indeed, multiscale roughness on the two-tier surface can greatly facilitate the droplet transport by virtue of less friction.

According to the contact line friction formula, the friction coefficient is the ratio of the driving force over the contact line velocity and it should be a constant [36]. It is notable that the contact line friction coefficient formula ($\xi = \frac{\gamma |cos\theta_s - cos\theta_d|}{U_c}$) was linearized with the assumption of $\frac{\gamma(cos\theta_s - cos\theta_d)\lambda^2}{2K_BT} \ll 1$. This assumption is only valid for small changes between static and dynamic contact angles ($\theta_s \approx \theta_d$). For negligible changes between static and dynamic contact angles, the relationship between the driving force and contact line velocity would be linear. Hence, the friction coefficients would be constant. But in the experiments, the difference between static and dynamic contact

angles is not always small. That is the reason that hyperbolic friction coefficients are obtained. As a future work, the author is going to extend the MKT theory to obtain a modified version of the friction coefficient formula which is valid for larger differences between static and dynamic contact angles.

The author of this thesis believes that his research has practical applications in the industry. It has been demonstrated that dropwise condensation of the water droplets on one-tier and two-tier structures can have potential applications in HVAC systems. It is noteworthy that the contact line friction coefficients found in this chapter can be applied to analyze the enhanced dropwise condensation on rough structures.

CHAPTER 6

CONCLUSION

In order to fully understand different wetting behaviors of the advancing and receding zones of liquid droplets on micro-patterned surfaces, a comprehensive analysis of the Wenzel-Cassie transition was performed. The author experimentally studied the Cassie regime to Wenzel regime transition on micropillar structures and found that the receding movement of a droplet on micropillars is more likely dominated by the Wenzel behavior with significant receding contact line pinning. According to the provided analysis, the receding motion on one-tier surfaces was in the Wenzel mode (highly sticky) and the strong receding contact line pinning led to a significant CAH on one-tier surfaces. The rolling mechanism plays the dominant role in the slippery behavior of the advancing contact line, which preferentially stays in the Cassie mode. Furthermore, the author studied the advancing and receding behaviors of water droplets on the micro-patterned surfaces with a full range of spacing factor. With a spacing factor higher than the receding transition point, both the advancing and receding movements follow the Cassie–Baxter model. However, with the spacing factor lower than the advancing transition point, the Wenzel behavior dominates both the advancing and receding motions. Owing to the high tendency of the advancing contact line to stay on top of micropillars the advancing movement remains less influenced by the roughness geometry for a wide range of spacing factors ($s_f^2 > 0.098$). Moreover, contact line oscillations of water droplets on smooth, one-tier, and two tier substrates were experimentally investigated. According to the results, the two-tier surface exhibits the lowest contact line fluctuations. This phenomenon was attributed to the existence of

Cassie-Baxter model on both advancing and receding movements of water droplet on two-tier substrate. However, the one-tier surface demonstrates a significant contact line pinning on the receding movement which leads to considerable oscillations. Finally, the author investigated the effects of surface roughness on contact line friction coefficients of water droplets on different types of hydrophobic surfaces. Advancing and receding CLFCs were measured, analyzed and compared on smooth, one-tier (with micropillars), and two-tier (with CNTs on micropillars) surfaces over a wide range of contact line velocities and droplet volumes. The provided measurements indicate that two-tier superhydrophobic surfaces with multiscale micro\nano-structures have the lowest advancing and receding CLFCs and can remarkably facilitate liquid movement. The advancing and receding CLFCs on the smooth surface are >10 times larger than those on the two-tier surface. However, the receding CLFC on the one-tier sample was found to be significantly larger than the advancing CLFC.

REFERENCES

[1]   C. Neinhuis and W. Barthlott, "Characterization and distribution of water-repellent, self-cleaning plant surfaces," *Annals of Botany*, vol. 79, pp. 667-677, 1997.

[2]   W. Barthlott and C. Neinhuis, "Purity of the sacred lotus, or escape from contamination in biological surfaces," *Planta*, vol. 202, pp. 1-8, 1997.

[3]   P. Wagner, R. Fürstner, W. Barthlott, and C. Neinhuis, "Quantitative assessment to the structural basis of water repellency in natural and technical surfaces," *Journal of Experimental Botany*, vol. 54, pp. 1295-1303, 2003.

[4]   B. Bhushan, and Y. C. Jung, "Micro-and nanoscale characterization of hydrophobic and hydrophilic leaf surfaces," *Nanotechnology*, vol. 17, p. 2758, 2006.

[5]   Z. Burton, and B. Bhushan, "Surface characterization and adhesion and friction properties of hydrophobic leaf surfaces," *Ultramicroscopy*, vol. 106, pp. 709-719, 2006.

[6]   N. A. Patankar, "Mimicking the lotus effect: influence of double roughness structures and slender pillars," *Langmuir*, vol. 20, pp. 8209-8213, 2004.

[7]   M. Sun, C. Luo, L. Xu, H. Ji, Q. Ouyang, D. Yu, and Y. Chen, "Artificial lotus leaf by nanocasting," *Langmuir*, vol. 21, pp. 8978-8981, 2005.

[8]   M. Nosonovsky, and B. Bhushan, "Biologically Inspired Surfaces: Broadening the Scope of Roughness," *Advanced Functional Materials*, vol. 18, pp. 843-855, 2008.

[9] S. Shibuichi, T. Onda, N. Satoh, and K. Tsujii, "Super water-repellent surfaces resulting from fractal structure," *The Journal of Physical Chemistry*, vol.100, pp. 19512-19517, 1996.

[10] K. Koch, B. Bhushan, and W. Barthlott, "Multifunctional surface structures of plants: an inspiration for biomimetics," *Progress in Materials Science*, vol. 54, pp. 137-178, 2009.

[11] W. J. Jeong, M. Y. Ha, H. S. Yoon, and M. Ambrosia, "Dynamic Behavior of Water Droplets on Solid Surfaces with Pillar-Type Nanostructures,". *Langmuir* , vol. 28, pp. 5360-5371, 2012.

[12] C. Dorrer, J. Rühe, "Advancing and receding motion of droplets on ultrahydrophobic post surfaces," *Langmuir* , vol. 22, pp. 7652-7657, 2006.

[13] D. Öner, T. J. McCarthy, "Ultrahydrophobic surfaces. Effects of topography length scales on wettability," *Langmuir*, vol.16, pp. 7777-7782, 2000.

[14] J. T. Cheng, A. Vandadi, and C. L. Chen, "Condensation heat transfer on two-tier superhydrophobic surfaces," *Applied Physics Letters*, vol. 101, pp. 131909-131909-4, 2012.

[15] Y. Jung, and B. Bhushan, "Wetting behaviour during evaporation and condensation of water microdroplets on superhydrophobic patterned surfaces," *Journal of microscopy*, vol. 229, pp. 127-140, 2008.

[16] R. N. Wenzel, "Resistance of solid surfaces to wetting by water," *Industrial & Engineering Chemistry,* vol. 28, pp. 988-994, 1936.

[17] A. Cassie, and S. Baxter, "Wettability of porous surfaces," *Transactions of the Faraday Society*, vol. 40, pp. 546-551,1944.

[18]   W. Choi, A. Tuteja, J. M. Mabry, R. E. Cohen, and G. H. McKinley, "A modified Cassie–Baxter relationship to explain contact angle hysteresis and anisotropy on non-wetting textured surfaces," *Journal of colloid and interface science*, vol. 339, 208-216, 2009.

[19]   D. Quéré, "Non-sticking drops," *Reports on Progress in Physics*, vol. 68, p. 2495, 2005.

[20]   G. McHale, N. Shirtcliffe, and M. Newton, "Contact-angle hysteresis on super-hydrophobic surfaces," *Langmuir*, vol. 20, pp. 10146-10149, 2004.

[21]   D. Quéré, A. Lafuma, and J. Bico, "Slippy and sticky microtextured solids," *Nanotechnology*, vol. 14, p. 1109, 2003.

[22]   L. Gao, and T. J. McCarthy, "Contact angle hysteresis explained," *Langmuir*, vol. 22, pp. 6234-6237, 2006.

[23]   A. Nakajima, K. Hashimoto, and T. Watanabe, "Recent studies on super-hydrophobic films," *Monatshefte für Chemie/Chemical Monthly*, *vol.*132, pp. 31-41, 2001.

[24]   L. Zhai, F. C. Cebeci, R. E. Cohen, and M. F. Rubner, "Stable superhydrophobic coatings from polyelectrolyte multilayers," *Nano Letters*, vol. 4, pp. 1349-1353, 2004.

[25]   M. Ma, and R. M. Hill, "Superhydrophobic surfaces," *Current Opinion in Colloid & Interface Science*, vol. 11, pp. 193-202, 2006.

[26]   A. Stalder, G. Kulik, D. Sage, L. Barbieri, and P. Hoffmann, "A snake-based approach to accurate determination of both contact points and contact angles,".

Colloids and surfaces A: physicochemical and engineering aspects, vol. 286, pp. 92-103, 2006.

[27]   D. Bonn, J. Eggers, J. Indekeu, J. Meunier, and E. Rolley, "Wetting and spreading,". *Reviews of modern physics*, vol. 81, p. 739, 2009.

[28]   C. Extrand, "Contact angles and hysteresis on surfaces with chemically heterogeneous islands," *Langmuir*, vol. 19, pp. 3793-3796, 2003.

[29]   M. Nosonovsky, and B. Bhushan, "Biomimetic superhydrophobic surfaces: multiscale approach," *Nano letters*, vol. 7, pp. 2633-2637, 2007.

[30]   L. Gao, and T. J. McCarthy, "The "lotus effect" explained: two reasons why two length scales of topography are important," *Langmuir*, vol. 22, pp. 2966-2967, 2006.

[31]   M. Voué, R. Rioboo, M. Adao, J. Conti, A. Bondar, D. Ivanov, T. D. Blake, and J. De Coninck, "Contact-line friction of liquid drops on self-assembled monolayers: chain-length effects," *Langmuir*, vol. 23, pp. 4695-4699, 2007.

[32]   M. J. De Ruijter, T. D. Blake, and J. De Coninck, "Dynamic wetting studied by molecular modeling simulations of droplet spreading," *Langmuir*, vol.15, pp. 7836-7847, 1999.

[33]   T. D. Blake, "The physics of moving wetting lines," *Journal of Colloid and Interface Science,* vol. 299, pp. 1-13, 2006.

[34]   H. Eral, and J. Oh, "Contact angle hysteresis: a review of fundamentals and applications," *Colloid and polymer science,* vol. 291, pp. 247-260, 2013.

[35]   R. A. Hayes, and J. Ralston, "The molecular-kinetic theory of wetting," *Langmuir, vol.* 10, pp. 340-342, 1994.

[36]   T. D. Blake, and J. De Coninck, "The influence of solid–liquid interactions on dynamic wetting," *Advances in colloid and interface science,* vol. 96, pp. 21-36, 2002.